AD-752 221

ANALYTICAL MODELING OF SUBSONIC PARTICLE EROSION

William F. Adler, et al

Bell Aerospace Company
Buffalo, New York

July 1972

AFML-TR-72-144

ANALYTICAL MODELING OF SUBSONIC PARTICLE EROSION

William F. Adler
George T. Sha

TEXTRON'S BELL AEROSPACE COMPANY

TECHNICAL REPORT AFML-TR-72-144

JULY 1972

Approved for public release; distribution unlimited.

Air Force Materials Laboratory
Air Force Systems Command
Wright-Patterson Air Force Base, Ohio

NOTICES

When Government drawings, specification, or other data are used for any purpose other than in connection with a definitely related Government procurement operation, the United States Government thereby incurs no responsibility for any obligation whatsoever; and the fact that the Government may have formulated, furnished, or in any way supplied the said drawings, specifications, or other data, is not to be regarded by implication or otherwise as in any manner licensing the holder or any other person or corporation, or conveying any rights or permission to manufacture, use, or sell any patented invention that may in any way be related thereto.

Copies of this report should not be returned unless return is required by security consdierations, contractual obligations, or notice on a specific document.

UNCLASSIFIED

Security Classification

DOCUMENT CONTROL DATA - R & D

(Security classification of title, body of abstract and indexing annotation must be entered when the overall report is classified)

1. ORIGINATING ACTIVITY (Corporate author) Bell Aerospace Company Buffalo, New York 14240	2a. REPORT SECURITY CLASSIFICATION Unclassified 2b. GROUP

3. REPORT TITLE

"Analytical Modeling of Subsonic Particle Erosion"

4. DESCRIPTIVE NOTES (Type of report and inclusive dates)

Summary June 1971 - June 1972

5. AUTHOR(S) (First name, middle initial, last name)

William F. Adler
George T. Sha

6. REPORT DATE July 1972	7a. TOTAL NO. OF PAGES ~~104~~ 115	7b. NO. OF REFS 21
8a. CONTRACT OR GRANT NO F33615-71-C-1528 b. PROJECT NO. 7342 c. Task No. 734202 d.	9a. ORIGINATOR'S REPORT NUMBER(S) 9b. OTHER REPORT NO(S) (Any other numbers that may be assigned this report) AFML-TR-72-144	

10. DISTRIBUTION STATEMENT

Approved for public release; distribution unlimited.

11. SUPPLEMENTARY NOTES Details of illustrations in this document may be better studied on microfiche	12. SPONSORING MILITARY ACTIVITY Air Force Materials Laboratory Air Force Systems Command Wright-Patterson AFB, Ohio 45433

13. ABSTRACT

An analytical approach to particle erosion of solid surfaces is developed based on a model of erosion pit nucleation and growth. The Hertzian theory of impact is used to introduce the kinematic and material parameters into this general statistical formulation of erosion processes. In order to minimize the number of unknown factors in the initial development of a predictive erosion theory, the particular case of solid spherical particles impacting directly on the plane surface of an elastic half-space is investigated.

Erosion tests were conducted on the AFML-Bell erosion apparatus in conjunction with the modeling studies. The erosion mechanisms in fused silica have been identified when eroded by multiple impacts of spherical glass beads. The erosion mechanism for 2.8 mil beads impacting at 200 fps was found to be different from the sequence of erosion mechanisms associated with 11 mil beads at the same velocity. The observed erosion mechanisms could be correlated with the measured erosion rates.

The erosion of fused silica can be modeled in terms of a preferential pit nucleation and growth. The quantitative evaluation of the statistical parameters in the erosion is being investigated. The controlled erosion tests provide evidence for the applicability of the Hertzian relations to the impact conditions of interest in solid particle erosion.

DD FORM 1 NOV 65 1473

UNCLASSIFIED

Security Classification

UNCLASSIFIED
Security Classification

14 KEY WORDS	LINK A ROLE	LINK A WT	LINK B ROLE	LINK B WT	LINK C ROLE	LINK C WT
Subsonic Erosion						
Solid Particles						
Analytical Modeling						
Brittle Materials						

UNCLASSIFIED
Security Classification

ANALYTICAL MODELING OF SUBSONIC PARTICLE EROSION

William F. Adler
George T. Sha

ic

FOREWORD

This report was prepared by Bell Aerospace Company, Buffalo, New York 14240, under Air Force Contract F33615-71-C-1528. It was initiated under Project No. 7342, "Fundamental Research on Macromolecular Materials and Lubrication Phenomena," Task No. 734202, "Studies on the Structure-Property Relationships of Polymer Materials."

The work was administered under the direction of the Air Force Materials Laboratory, Air Force Systems Command, Wright-Patterson Air Force Base, Ohio, with George F. Schmitt, Jr. of the Elastomers and Coatings Branch, Nonmetallic Materials Division, acting as project engineer.

This report covers the work carried out during the period from June 1971 through June 1972 and was submitted by the authors in June 1972.

This technical report has been reviewed and is approved.

WARREN P. JOHNSON, Chief
Elastomers and Coatings Branch
Nonmetallic Materials Division
Air Force Materials Laboratory

ABSTRACT

An analytical approach to particle erosion of solid surfaces is developed based on a model of erosion pit nucleation and growth. The Hertzian theory of impact is used to introduce the kinematic and material parameters into this general statistical formulation of erosion processes. In order to minimize the number of unknown factors in the initial development of a predictive erosion theory, the particular case of solid spherical particles impacting directly on the plane surface of an elastic half-space is investigated.

Erosion tests were conducted on the AFML-Bell erosion apparatus in conjunction with the modeling studies. The erosion mechanisms in fused silica have been identified when eroded by multiple impacts of spherical glass beads. The erosion process for 2.8 mil beads impacting at 200 fps was found to differ from the sequence of erosion mechanisms associated with 11 mil beads at the same velocity. The observed erosion mechanisms could be correlated with the measured erosion rates.

The erosion of fused silica can be modeled in terms of a preferential pit nucleation and growth process. The quantitative evaluation of the statistical parameters in the erosion model is being investigated. The controlled erosion tests provide evidence for the applicability of the Hertzian relations to the impact conditions of interest in solid particle erosion.

TABLE OF CONTENTS

		PAGE
I.	INTRODUCTION	1
II.	SUMMARY	3
III.	DEVELOPMENT OF GENERAL EROSION THEORY	8
IV.	SOLID PARTICLE IMPACTS ON BRITTLE MATERIALS	17
	A. Hertizan Theory of Impact	18
	B. Fracture of Glass Surfaces by Spherical Indenters	25
V.	DESCRIPTION OF EROSION EXPERIMENTS	30
	A. Experimental Procedures	30
	B. Erosion Mechanisms in Fused Silica	44
VI.	GENERAL DISCUSSION	90
VII.	CONCLUSIONS	96
APPENDIX	COMPUTER PROGRAM FOR ANALYTIC MODELING	98
REFERENCES		103

LIST OF ILLUSTRATIONS

FIGURE		PAGE
1	An Idealization of Erosion Through the Nucleation and Growth of Pits in Successive Layers of An Eroding Solid	9
2	Glass Erosion Test Specimens	31
3	Glass Beads Used in Erosion Experiments	33
4	Sand Injection and Exhaust System for AFML-Bell Erosion Apparatus	36
5	Variation of Density of 3-Mil Fracture Rings on the Surface of Specimen G1 as a Function of Exposure Time	46
6	Erosion in the Vicinity of 3-Mil Ring Fractures on Specimen G1	48
7	Erosion in the Vicinity of A Large 6 Mil Pit on Specimen G1	52
8	Erosion in the Vicinity of a Spalled Region on Specimen G1	56
9	0.9 Mil Ring Fractures on the Surface of Specimen G1	58
10	Weight Loss Data for Specimen G1	61
11	Weight Loss Data for Specimen G2	63
12	Weight Loss Data for Specimen G3	64
13	Ring Fractures on the Surface of Specimen G2 After Impact by 11 Mil Beads for 1 Second	65
14	Ring Fractures on the Surface of Specimen G3 After Impact by 11 Mil Beads for 1 Second	66
15	Ring Fracture on Specimen G2 After an Exposure Time of 1 Second	68
16	Ring Fracture on Specimen G2 After 15 Seconds Exposure Time	69
17	Details of Ring Fractures on Specimen G3 After an Exposure Time of 1 Second	70
18	Details of Ring Fractures on Specimen G3 After an Exposure Time of 3 Seconds	71

LIST OF ILLUSTRATIONS

FIGURE		PAGE
19	Ring Fractures in Pyrex Impacted by 11 Mil Glass Beads at 300 fps	73
20	Overlapping and Nearly Overlapping Rings Fracture in Pyrex Impacted by 11 Mil Beads at 400 fps	75
21	Subsurface Fracture Interactions in Pyrex Impacted by 11 Mil Beads at 400 fps	75
22	Subsurface Fracture Interaction in Pyrex Impacted by 11 Mil Beads at 400 fps	76
23	Appearance of the Surface of Specimen G2	78
24	Distribution of Diameters of Ring Fractures in Specimen G2	79
25	Distribution of Diameters of Ring Fractures in Specimen G3	80
26	Mechanism for Removal of Cone Fractures from Surface	82
27	Removal of Fractured Glass from Interstitial Regions on Surface of Specimen G2	84
28	Growth of Area of Interstitial Glass Removal on Surface of Specimen G2	84
29	Appearance of Eroded Surface of Specimen G2 at 130 Seconds	86
30	General Appearance of Eroded Surface of Specimen G2 and G3	88
31	Appearance of Eroded Surface of Specimen G2 at 305 Seconds	89

LIST OF TABLES

TABLE		PAGE
I	Mechanical Properties of Fused Silica and Soda Lime Glass	34
II	Erosion Test Schedule	35
III	Hertizan Impact Parameters For Fused Silica	42

I. INTRODUCTION

The erosion of engineering materials moving through rain, sand, and dust environments poses serious operational and maintenance problems in a variety of military and commerical systems. To counter this problem, the Air Force Materials Laboratory has established programs of erosion research to develop advanced erosion test apparatus, to characterize the erosion of aerospace materials in known environments, to establish the basic mechanics of erosion of engineering materials, and to develop new aerospace materials having improved erosion resistance.

The complexity of the loading conditions associated with erosive environments and the lack of knowledge of the general behavior of material surfaces subjected to these loading conditions have been major obstacles to the detailed analysis of erosion phenomena. In order to confront this pacing problem, attention in this report has been focused on the simplest combination of circumstances which lead to a realistic model of the erosion process for particle impacts.

The development of mechanistically sound erosion models complements the overall Air Force erosion research effort in two ways. First, such models, even if only approximate, will help

significantly in the extrapolation of erosion test results to service conditions, and hence facilitate the engineering choice of materials for use in particular service environments. Second, the development of mechanistically sound erosion models will allow estimations to be made of the relative importance of the various particle, material, and interaction parameters which influence the complex, cumulative process of erosion, and hence aid in the interpretation of erosion mechanism studies and in the design of new materials or coatings having improved erosion resistance in specific service environments.

II. SUMMARY

The erosion of brittle materials by multiple, solid particle impacts has been idealized as a process of pit nucleation and growth on the surface of the eroding solid. An analytical model is developed based on the assumption that the erosion pits are rather uniform in depth during the initial stages of growth and that typical pits undergo appreciable lateral growth before conjoining with other growing pits. The eroding solid is considered to be a laminate of plates whose individual thickness is determined by the depth of propagation of typical impact fractures. The governing equations have been programmed for digital computer computations of the erosion rates and weight loss as functions of exposure time.

The mathematical formulation requires the specification of a time-dependent pit nucleation probability function and growth rate for each layer of the laminated model of the eroding solid. The value of the theory as a predictive tool in the development of erosion resistant materials depends on how much information pertaining to the kinematics of the eroding environment and the materials characteristics of the eroding solid can be incorporated into the explicit analytic representation of the pit nucleation and growth rate functions. The direct impact of small, spherical

glass beads on the plane face of relatively flaw-free fused silica (Corning 7940) samples was investigated in order to minimize the number of unknown factors pertaining to the kinematic and material parameters. The impact conditions were selected so that results from the Hertzian theory for the impact of a spherical elastic body on an elastic half-space could be used.

The pit nucleation concept is dependent on the manner in which the material's surface is fractured by the multiple solid particle impacts. The nucleation of an erosion pit may occur through one of several processes whose relative probabilities are difficult to access without evaluating a detailed model. This information was obtained through microscopic observations of the erosion mechanisms in a series of controlled experiments using the AFML-Bell erosion apparatus.

Three erosion tests were conducted on fused silica samples: 2.8 mil beads impacting at 200 fps; 11 mil beads impacting at 200 fps; and 11 mil beads impacting at 300 fps. The experimental program was designed to obtain information on the erosion mechanisms, to obtain explicit forms of the pit nucleation and growth rate functions, and to obtain weight loss data for comparison with the predictions of the theory.

Entirely different erosion mechanisms were found for the 2.8 and 11 mil beads. The nucleation of pits on the surface of the fused silica specimen impacted by 2.8 mil beads was due to the production and intersection of ring fractures which were on the order of one mil in diameter. Material was removed from the surface layer to a maximum depth of 10 microns by the formation of irregularly-shaped pits. The growth of the nucleated areas was preferential in accordance with the erosion model.

When the 11 mil beads were used, there was a much higher probability for the production of conical fracture subsurfaces. The average diameter of the inner ring fracture seen on the surface of the specimen was about 2.5 mils. As the number of damaging impacts increased, the subsurface fractures became more obvious. No new ring fractures were formed in the interstitial regions between the ring fractures produced during the early stages of the erosion process. Instead a very dense network of internal fractures developed with very little material removal. At a certain point in the development of these fractured regions, material was removed to a depth of 60 microns for impacts at 200 fps and 90 microns for impacts at 300 fps. This was a nucleation and growth process, although the regions observed were quite erratic in their growth patterns. The interstitial material was removed at a higher erosion rate than the one prevailing before this began. After most of the interstitial material was removed, the

eroded surface consisted of a continuous array of conical frustums protruding from the bulk material. The majority of the plateau regions were still unaffected by the particle impacts and the side surfaces were quite smooth. At this point, material was removed at a uniform rate by the fine-scale chipping of the plateau regions of the frustum population. The time of occurrence of the observed erosion mechanisms can be correlated with the weight loss data.

The diameters of the ring fractures in all three tests were found to be in general agreement with the Hertzian predictions for the impact conditions used in these experiments. The development of a suitable fracture criterion will require further study; however, on the basis of the results obtained here, the energy balance approach is preferable to the statistical flaw theories.

An experimental procedure was devised for direct evaluation of the pit nucleation and growth rate functions. In the case of the 2.8 mil beads, a number of ring fractures with a diameter of 3 mils were observed on the surface of the sample and were judged to be the major contributor to material removal. The fine-scale chipping due to the smaller ring fractures was considered to be of secondary importance. At an intermediate stage of the erosion process the frequency of occurrence of the larger rings approached zero. It was then discovered that the fine-scale chipping was the principal erosion mechanism. There was no growth

of the eroded regions associated with the 3 mil rings. No useful data were obtained pertaining to the evaluation of the statistical parameters for this test. The reason for the occurrence of the anomalous 3 mil ring fractures is being investigated.

The erosion behavior of the multiple impacts of the 11 mil beads was somewhat unexpected. The experimental procedure for evaluating the statistical parameters was not suitable for this purpose. Alternative procedures for obtaining the necessary data for the model calculations are being considered.

III. DEVELOPMENT OF GENERAL EROSION THEORY

An analytical model for describing erosion processes in materials which erode by the nucleation and growth of pits in the material surface is currently under development. The eroding solid is represented by a laminate of individual plates as shown in Fig. 1. The thickness of each plate is determined by the mean pit depth for the pits which are formed at each stratum in the solid. Assume erosion initiates through the nucleation and growth of flat-bottomed pits which penetrate the topmost plate (Fig. 1). Erosion of the next lower plate proceeds through the nucleation and growth of similar pits over that portion of the plate surface which has been exposed to erosive impact through regression of the upper plate (Fig. 1). Erosion of this plate exposes a portion of the surface of the next lower plate, which erodes in the same way to expose a portion of the surface of the next lower plate, and so on.

Consider first the erosion of the topmost lamella of the material. Let the thickness of the plate be D and its surface area be A. Let the surface be exposed to erosion at time zero. Presume that the probability that an erosion pit will be formed in an arbitrary unit area of surface in the time interval between

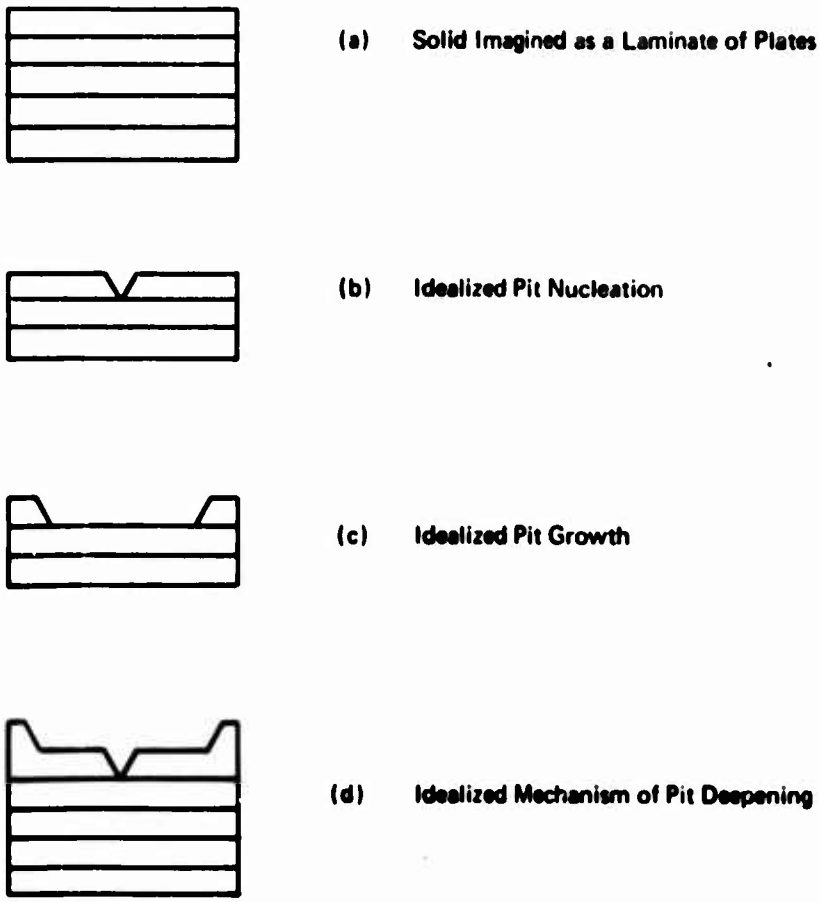

Figure 1. An Idealization of Erosion through the Nucleation and Growth of Pits in Successive Layers of an Eroding Solid

the times τ and $\tau + d\tau$ after initial exposure is known and is given by the expression $I_1(\tau)d\tau$. The function $I_1(\tau)$ is restricted in that it must be integrable and must vanish in the domain $\tau \leq 0$. Further assume that the pit nuclei have negligible volumes and they grow uniformly over the surface at a constant rate G, removing material to depth D with each increment of growth.

If erosion pits are small and so dispersed over the surface that they do not impinge on one another, then a pit nucleated at time τ will have grown to cause the removal of a volume δv at time t.

$$\delta v_1(t,\tau) = DG_1^2(t-\tau)^2 \tag{1}$$

where G_1 is the lateral growth rate for the first layer. It is assumed that the eroded area at the bottom of a nucleated erosion pit at depth D is the same as at the surface. It is unlikely that this will be the case in actual erosion processes. The influence of the shape of a nucleated erosion pit on the volume of material removed will be taken into account after microscopic observations of eroded surfaces indicate the form of the shape factor adjustment required. The volume removed at time t due to the growth of all pits nucleated in the time interval $(\tau,\tau+d\tau)$ is then

$$\delta V_1(t,\tau) = AI_1(\tau)\delta v_1(t,\tau)d\tau \tag{2}$$

However, after significant erosion takes place, the uneroded surface area is much less than the total surface area A, and so the number of new pits nucleated is much smaller than the number given by $AI_1(\tau)d\tau$. Also growing pits may coalesce with one another to

form single larger pits. To account for these effects, we use the net uneroded area at any instant τ in calculating the number of pits nucleated in the time interval $(\tau,\tau+d\tau)$. Hence, Eq. (2) becomes,

$$\delta V_1(t,\tau) = G_1^2(t-\tau)^2 I_1(\tau)(V-\Delta V_1(\tau)) \qquad (3)$$

where $\Delta V_1(\tau) = D\Delta A_1(\tau)$ is the total volume eroded from the start of the erosion process to time τ and $\Delta A_1(\tau)$ is the eroded surface area associated with the same time interval. At present $\Delta V_1(\tau)$ is an unknown quantity. $V = AD$ is the volume of the first plate. Integrating Eq. (3) from $(0,t)$,

$$\Delta V_1(t) = G_1^2 \int_0^t (t-\tau)^2 I_1(\tau)[V-\Delta V_1(\tau)]d\tau \ , \qquad (4)$$

yields a Volterra integral equation of the second kind for determining the total eroded volume of the first layer at time t due to all the pits nucleated during the total time of exposure to the eroding environment.

We follow a similar procedure for evaluating the volume eroded from the second layer, except that the surface of layers below the first is only gradually exposed to the erosive environment. For convenience of presentation, let us assume that the

mean pit depth is also D for the second layer. In accordance with earlier considerations the net exposed area on the surface of the second layer at any time ψ is $\Delta A_1(\psi) - \Delta A_2(\psi)$ where $\Delta V_2(\psi) = D\Delta A_2(\psi)$ is the unknown quantity which must be determined. The amount of new area which is exposed during a time interval $(\psi,\psi+d\psi)$ can be expressed in terms of a Taylor's expansion,

$$[\Delta A_1(\psi+d\psi) - \Delta A_2(\psi+d\psi)] - [\Delta A_1(\psi)-\Delta A_2(\psi)]$$

$$\simeq \frac{d\Delta A_1(\psi)}{d\psi}\, d\psi - \frac{d\Delta A_2(\psi)}{d\psi}\, d\psi \qquad (5)$$

The number of pits nucleated at time τ due to new area exposed during the time interval $(\psi,\psi+d\psi)$ is given by

$$\delta n(\tau,\psi) = I_2(\tau-\psi)\left(\frac{d\Delta A_1(\psi)}{d\psi} - \frac{d\Delta A_2(\psi)}{d\psi}\right) d\psi \qquad (6)$$

It should be noted that a different pit nucleation function is specified for the second layer. The total number of pits nucleated at time τ is

$$n(\tau) = \int_0^{\tau} \delta n(\tau,\psi)d\psi \qquad (7)$$

Then the volume removed from the second layer at time t due to all the pits present at time τ will be

$$\delta V_2(t,\tau) = DG_2^2(t-\tau)^2 n(\tau) \tag{8}$$

where the linear growth rate on the second layer is taken to be different from that on the first. Combining Eqs. (6) to (8) and integrating with respect to τ, we find that the total volume eroded from the second layer at time t is simply

$$\Delta V_2(t) = G_2^2 \int_0^t (t-\tau)^2 \int_0^\tau I_2(\tau-\psi) \cdot \left(\frac{d\Delta V_1(\psi)}{d\psi} - \frac{d\Delta V_2(\psi)}{d\psi}\right) d\psi d\tau \tag{9}$$

Or finally, Eq. (9) can be put into a more convenient form by differentiation with respect to t,

$$\frac{d\Delta V_2(t)}{dt} = 2\, G_2^2 \int_0^t (t-\tau) \int_0^\tau I_2(\tau-\psi) \cdot \left(\frac{d\Delta V_1(\psi)}{d\psi} - \frac{d\Delta V_2(\psi)}{d\psi}\right) d\psi d\tau \tag{10}$$

Eq. (10) is slightly more complicated than Eq. (4); but once $\Delta V_1(\psi)$ is found from Eq. (4), it can be inserted in Eq. (10) for evaluating $\frac{d\Delta V_2(t)}{dt}$.

The derivation of the equations governing material removal from subsequent layers proceeds in a manner analogous to that for the second layer. In summary, the calculation of the weight loss (or rate of erosion) experienced by a material body subjected to an erosive environment requires solving the following system of equations.

$$\left.\begin{aligned} \Delta V_1(t) &= G_1^2 \int_0^t (t-\tau)^2 I_1(\tau)[V-\Delta V_1(\tau)]d\tau \\ \frac{d\Delta V_\alpha(t)}{dt} &= 2\, G_\alpha^2 \int_0^t (t-\tau) \int_0^\tau I_\alpha(\tau-\psi)\cdot \\ &\qquad \left(\frac{d\Delta V_{\alpha-1}(\psi)}{d\psi} - \frac{d\Delta V_\alpha(\psi)}{d\psi}\right) d\psi d\tau \end{aligned}\right\} \quad (11)$$

where $\alpha = 2,3,\ldots,N$, and

$$\Delta W(t) = \rho\Delta V(t) = \rho \sum_{\alpha=1}^{n} \Delta V_\alpha(t) \quad (12)$$

is the total weight loss at any time t.

The system of equations has been programmed for digital computer computations. These computations are extremely efficient, since a considerable simplification in their numerical evaluation was obtained through an observation pertaining to the general form of the equivalent system of finite-difference equations. There is a considerable degree of flexibility in the functional form of the pit nucleation probabilities, the growth rates, and mean pit depths, since the computer code is not restricted in this regard. The explicit details of the deviation of Eq. (11) can be readily modified when experimental observations indicate that such modifications are in order. The computer program is provided in the Appendix.

Heymann[12] developed a conceptually-similar model which incorporated the nucleation and growth of eroding areas in terms of a log-Normal frequency distribution function. Heymann demonstrated that qualitative agreement can be obtained with various forms of experimental erosion rate-time curves through proper selection of the parameters in the distribution function. His model can only describe the erosion data once it is obtained. The model developed here could be used for a similar purpose.

The problem of analytically determining the erosion of a material which behaves according to our model is reduced to the problem of specifying nucleation and growth kinetics for erosion pits. The value of this model's calculations as a predictive

tool in the development of erosion resistant materials depends on how much information pertaining to the kinematics of the erosive environment and the material characteristics of the eroding solid can be incorporated into the explicit analytic representation of the pit nucleation and growth rate functions. It would be satisfying to prescribe these functions on a purely analytical basis; however, this is not possible at the present time. This research considers the relevant analytical approaches in conjunction with a series of controlled erosion tests.

IV. SOLID PARTICLE IMPACTS ON BRITTLE MATERIALS

The statistical parameters required in the erosion theory developed in the previous section can be obtained by the direct observation of pit nucleation and growth in materials which erode in this manner. However, the predictive character of the model is greatly enhanced if the kinematic parameters associated with specific erosion conditions and material properties for general material classes can be introduced into the general formulation. In order to accomplish this objective, the general erosion model is applied to the simplest conditions of solid particle impacts on brittle materials. The initial evaluation of the erosion model will be based on the following assumptions:

(1) The eroded solid can be represented by a semi-infinite half-space which initially has a perfectly plane surface.

(2) The eroded solid is a linearly elastic material which is homogeneous and isotropic.

(3) The eroding particles are spherical in form.

(4) The eroding particles are homogeneous and isotropic linearly elastic solids.

(5) The impact velocities are low enough that the Hertzian theory of impact is applicable.

(6) The eroding particles only collide with the eroded solid in a direction which is perpendicular to its initially plane surface.

In order to make the analysis of the particle impacts as manageable as possible, it is desirable to work within the domain of the Hertzian theory of impact which is one of the few analytical approaches to impact phenomena that can be handled without the aid of elaborate computer codes. This choice allows us to take advantage of the extensive prior theoretical and experimental work on Hertzian impacts of purely elastic bodies.

Inorganic glasses were considered to be most representative of the idealized brittle, elastic materials required in the Hertzian analysis. For the experimental studies of the erosion mechanisms and erosion characteristics under the prescribed conditions, fused silica (Corning 7940) was selected for the glass specimens and soda lime glass beads are being used for the impacting particles. The criteria for fracture initiation of glass surfaces loaded by spherical indenters is also considered in this section.

A. HERTZIAN THEORY OF IMPACT

Since much of the discussion which follows is based on the results of the Hertizan theory of impact, the pertinent aspects of this theory will be presented for future reference. Hertz[3,4] assumed that the collision of two bodies could be regarded as a statical problem; the compression at the place of contact is regarded as gradually produced and as subsiding completely by reversal of the process by which it was produced. Hertz theory

of impact for perfectly elastic bodies does not account for dissipation of energy; therefore, no loss in the total kinetic energy of the two bodies will occur. This restriction has been relaxed in more recent analyses of the impact of a spherical indenter on a viscoelastic half-space.

The problem originally considered by Hertz was to determine for the case of two elastic isotropic bodies which touch each other over a very small part of their surface and exert upon each other a finite pressure, distributed over the common area of contact, the form of the common surface, the distribution of pressure over it, and a relation between the distance the bodies approach each other and the pressure existing on the contacting surface of each body. The results given here will be restricted to the case of a spherical elastic body indenting an elastic half-space. A detailed account of the stress distribution for this case was first given by Huber[5]: the specialized theory is often referred to as the Hertz-Huber theory.

Hertz makes the following simplifying assumptions:

(a) The surface of contact is always small in comparison with the dimensions of the bodies involved.

(b) The surfaces in contact are imagined as perfectly smooth, i.e. we assume that only a normal pressure acts between the parts in contact.

To apply the static theory to the impact of perfectly elastic bodies the following additional assumptions were made by Hertz:

(c) ...the elastic state of the two bodies near the point of impact during the whole duration of impact is very nearly the same as the state of equilibrium which would be produced by the total pressure subsisting at any instant between the two bodies, supposing it to act for a long time.

Thus, no account of vibrations present in the bodies due to impact was undertaken, and the pressure between the two bodies is assumed to be gradually applied even though the entire time the bodies are in contact is relatively short.

(d) ...the time of impact is also large compared with the time taken by elastic waves to traverse the impinging bodies from end to end.

The problem under consideration becomes that of an elastic body subjected to a pressure distributed over a very small portion of its surface. Hertz thus reduced the problem to the

the case of a body bounded by an infinite plane which is appropriate if the dimensions of the body are large compared with those of the area of the load.

The radius a of the circle of contact and the distance of approach α of the two bodies are then given by

$$a = \left(\frac{3}{4} PR\,(k_1 + k_2)\right)^{1/3} \tag{13}$$

$$\alpha = \left(\frac{9}{16}\,\frac{P^2(k_1 + k_2)^2}{R}\right)^{1/3} \tag{14}$$

where P is the normal load on the indenter, R is the indenter radius, and

$$k_1 = \frac{1-\nu_1^2}{E_1}, \quad k_2 = \frac{1-\nu_2^2}{E_2} \tag{15}$$

are the elastic moduli for the sphere and half-space, respectively, (ν is Poisson's ratio and E is Young's modulus). If the magnitude of the maximum pressure is scaled to the radius of the contract area, the pressure distribution over the contact area is shown to be hemispherical for the particular case under consideration.

Having the magnitude of the contact surface and the pressure acting on it, the elastic stress distribution in the

half-space can be evaluated[6]. Simple formulas for the stress components can only be obtained along the axis of symmetry (the positive z-axis directed into the interior of the half-space) and over the plane surface of the half-space. The determination of the stress components at other points in the half-space requires numerical analysis. The radial tensile stress on the surface of the half-space outside the contact area is

$$\sigma_r = \frac{(1-2\nu_2)}{2\pi} \frac{P}{r^2} \qquad (r \geq a) \qquad (16)$$

The radial stress is compressive for $r \geq a$. The circumferential component of the stress σ_θ is compressive over the entire surface and of the same magnitude as σ_r for $r \geq a$. Along the z-axis (axis of symmetry) σ_r, σ_θ, and σ_z are all compressive between the surface and a critical depth which deperds on ν. At this critical depth both σ_r and σ_θ vanish and are tensile for all greater depths. The σ_z stress component is compressive at all depths along the axis.

The maximum radial tensile stress is located at the circular boundary of the contact surface, Eq. (16), and has a magnitude of

$$(\sigma_r)_{max} = \frac{1-2\nu_2}{\pi(3(k_1+k_2))^{2/3}} P^{1/3} R^{-2/3} \qquad (r = a) \qquad (17)$$

To study the impact of a spherical body on an elastic surface, the previous relations from the Hertzian theory are restated in terms of the velocity of approach v instead of the load P which is now an unknown. In order to establish a relation between P and v, the kinetic energy of the impacting sphere is equated to the strain energy at the time of maximum impression.

$$\frac{1}{2}\left(\frac{4}{3}\ \rho_1 \pi\ R^3\right) v^2 = \int_0^{\alpha_{max}} P(\alpha)d\alpha$$

where ρ_1 is the density of the impacting sphere. Using Eq. (14),

$$P_{max} = \frac{4}{3}\left(\frac{5}{4}\ \pi\rho_1\right)^{3/5}(k_1 + k_2)^{-2/5}\ v^{6/5}\ R^2 \qquad (18)$$

The duration of contact T between the two impacting bodies is given by

$$T = 2.943\left[\frac{5}{4}\ \pi\rho_1\ (k_1 + k_2)\right]^{2/5} \frac{R}{v^{1/5}} \qquad (19)$$

The results of the Hertzian theory of impact have been investigated experimentally since the time of Hertz and have been confirmed for a broad range of materials and impact conditions[7]. The greatest deviations from the Hertizan predictions occur in the case of very small diameter spheres impacting on a plane surface

which is particularly relevant to solid particle erosion. As the duration of contact decreases, either due to impact by small particles or high impact velocities, the dynamic effects of the impact must be taken into account.

B. FRACTURE OF GLASS SURFACES BY SPHERICAL INDENTERS

In a theory of erosion for brittle materials through repeated Hertzian impacts, the dominant consideration is how the Hertzian stress distribution influences the nucleation and propagation of brittle fractures. If an elastic sphere is pressed onto an elastic surface containing a dense distribution of fine flaws under steadily increasing load, no appreciable crack propagation is observed until the load exceeds a critical magnitude P_c. The evaluation of the critical fracture load for a spherical indenter pressed against a glass plate has been an active area of research since the time of Hertz.

The crack produced quasistatically in a large glass plate by a spherical indenter appears as a ring on the surface and spread out below the surface to form the frustrum of a cone. Once a fracture is formed, however, the stress distribution is modified, since the fracture surfaces act as free boundaries for which the normal stress is zero: the Hertz-Huber analysis will no longer be valid. In this regard, it is noted however that Sheldon and Finnie[8] have provided experimental evidence that the Hertzian expression for the distance of approach between a 1/8 in. diameter steel sphere impressing a pyrex glass plate is not appreciably in error even after the application of loads in excess of 120 times the initial fracture load and multiple ring fractures were formed.

The Hertz-Huber equations give an accurate representation of the stress distribution in glass plates before fracture initiates. From Eq. (17) the maximum radial tensile stress is located at the circular boundary of the contact surface for the inhomogeneous stress distribution. In the case of brittle materials, such as glass, a simple fracture criterion is that failure will occur when a critical value of the maximum tensile stress is reached. If the tensile strength of glass is assumed to be constant, then, according to Eq. (17), the load P_c required to produce cracking should vary with the square of the indenter radius. This relation, P_c proportional to R^2, has been confirmed experimentally for large sphere radii (minimum radii on the order of one inch). However, Auerbach[9] found that as the radius of the indenter decreased, the magnitude of the critical load for fracture increased in direct proportion to R. The relation

$$P_c/R = H \text{ (a constant)} \tag{20}$$

has been designated Auerbach's law by Roesler[10]. Substitution of this relation into Eq. (17) means that the fracture stress varies as the one-third power of the indenter radius. The observed size effect in the fracture of glass has led to considerable controversy as to the physical explanation of Auerbach's law.

One explanation of this size effect in glass is based on modification of Griffith's criterion for brittle fracture applied to flaws in glass surfaces. The modification takes into account the fact that the stress required to initiate a fracture from a particular flaw in brittle materials depends on the size, location, and orientation of the flaw in the inhomogeneous stress field produced by a spherical indenter on a plate. It is then conjectured that a larger stressed area (larger indenter radius) has a greater probability of including a particularly weak flaw. However, as Roesler[10] points out, according to this reasoning the scatter in the evaluation of the critical load should increase as the size of the radius of the indenter decreases. This scatter is not observed experimentally; the scatter in the evaluation of the critical load is the same for small as well as large indenters. Statistical theories of fracture from assumed surface flaw distributions in a Hertzian stress field have been advanced recently by Tsai and Kolsky[11], Oh and Finnie[12], and Fisher[13]. Fisher demonstrates that a particular form of flaw distribution is required to obtain the Auerbach relation, Eq. (20). It is highly improbable that special forms of the flaw distribution are present in all of the glass samples tested.

An alternative theoretical treatment of the problem has been developed by Frank and Lawn[14], who employ Roesler's energy scaling criterion[10]. Roesler showed that the various

empirical relations for the production of cone cracks can be put into the form that just before fracture the elastically stored energy is proportional to the area of the circle of contact. Since cone cracks are geometrically similar, scaling to the circle of contact, Roesler suggested that the fundamental form of Auerbach's law is the proportionality between the elastically stored energy and the crack surface area. Frank and Lawn[14] studied conditions for the instability of embedded cracks of the Griffith type in the inhomogeneous Hertzian stress field. They developed a procedure for determining stress intensity factors at the tips of these flaws and the energy release on incremental crack propagation. These relations were used to obtain criteria for Hertzian fracture which predict behavior substantially in accord with experiment and lead to estimates of the surface tension of fracture surfaces in glass which are in reasonable agreement with those obtained through other techniques.

Langitan and Lawn[15] compared the predictions of the flaw statistical theories and the energy balance theory of Frank and Lawn for abraded glass surfaces which can be assumed to contain a uniform distribution of flaws. They demonstrate that the experimental evidence does not conform to the results of the flaw statistical theory for this particular case which provides an explicit representation for the flaw distribution. According to the flaw statistical theories there should be no difficulty in

encountering a critical flaw; however, it is found experimentally that the fracture load is greater than that evaluated for as-received glass surfaces.

Results from the energy balance approach are being considered in conjunction with establishing fracture criteria for the impact conditions which are of interest in erosion processes. The production of ring fractures on the glass surfaces by multiple particle impacts is the elemental fracture mechanism in this study, however a single ring fracture may or may not be the nucleus for a growing erosion pit. The nucleation of an erosion pit may occur through one of several processes whose relative probabilities are difficult to assess without evaluating a detailed model. Thus, the critical step in the nucleation of an erosion pit may be the impact of a sphere causing a ring fracture in the immediate neighborhood of a previously formed ring fracture, it may require three adjacent ring fractures, and more complex nucleating steps may easily be imagined. Thus the probability of pit nucleation as a function of time of exposure to erosion must be determined through an experimental study of the dominant pit nucleation mechanism in conjunction with the analyses of Hertzian impact. The experimental study is described in the next section.

V. DESCRIPTION OF EROSION EXPERIMENTS

The experimental program is designed to evaluate the damage to the eroded surface of fused silica specimens after incremental exposures to the direct impact of spherical glass beads in the AFML-Bell erosion apparatus. A procedure is established for evaluating the statistical parameters required in the theory, and the fundamental mechanisms for the nucleation of pits in fused silica are determined experimentally.

A. EXPERIMENTAL PROCEDURES

Due to the low impact velocities used in this study, it was possible to design specimens with a sizable flat surface exposed to the eroding particles. This geometry eliminated the effect of the variable angles of attack associated with the aerodynamic shapes usually employed in the AFML-Bell erosion apparatus. A special sample holder was fabricated for the rotating arm so that these flat-faced specimens could be used. Fused silica (Corning 7940) was selected for the erosion targets. The general specimen dimensions are indicated in Figure 2. The diameters of the glass beads (impacting particles) were selected so that they would be small in comparison with lateral dimensions of the specimen. Under these conditions the effects of the impacts will be quite

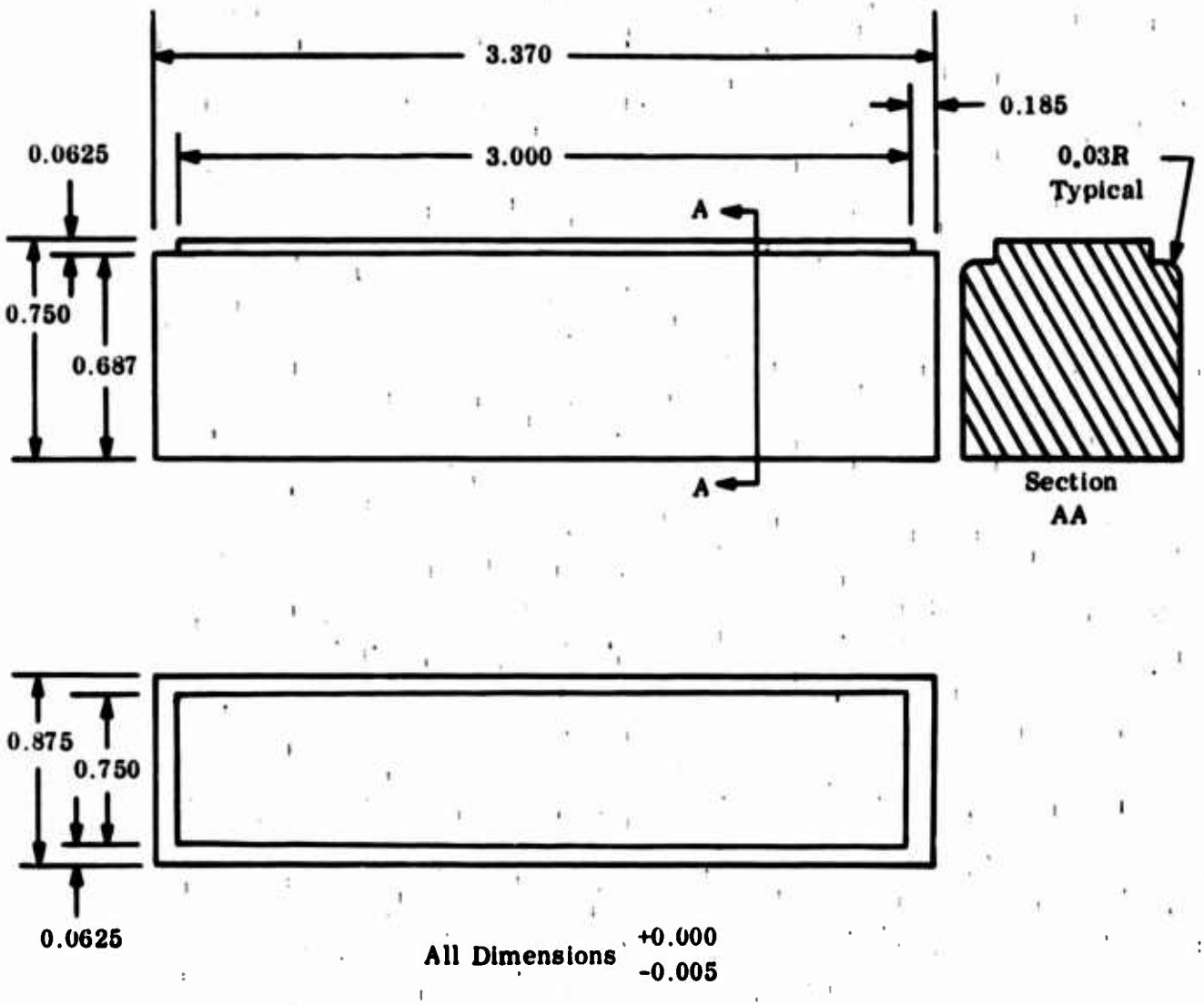

Figure 2. Glass Erosion Test Specimens

localized; the influence of the finite boundaries of the specimen will be minimized, and the central region of the specimen would approximate a mathematical half-space as required in the Hertzian analysis. In order to provide an accurate appraisal of the model, spherical glass beads (3M Superbrite-Knoop Hardness No. 525) with diameters of 2.8 mils (70μ) and 11.4 mils (290μ) were used. The beads showed some variation in size from these dimensions, but the size distribution was quite narrow around the diameter indicated. A comparison of the two bead sizes and the extent of their sphericity can be seen in Figure 3. The mechanical properties of the fused silica (Corning 7940) and the glass beads are provided in Table I.

The test conditions for the fused silica samples are given in Table II. Particle impact velocities of 200 and 300 fps were selected on the basis of adjunct experimentation using pyrex samples. Impact velocities were required which would be capable of producing ring fractures on the surface of the fused silica but were not of a magnitude that the initial and intermediate stages of the erosion process would be completed before the required statistical data were obtained.

In the erosion experiments conducted in the AFML-Bell erosion apparatus shown in Figure 4, the glass beads are taken from the sand hopper by a screw-type feeder and fall down the

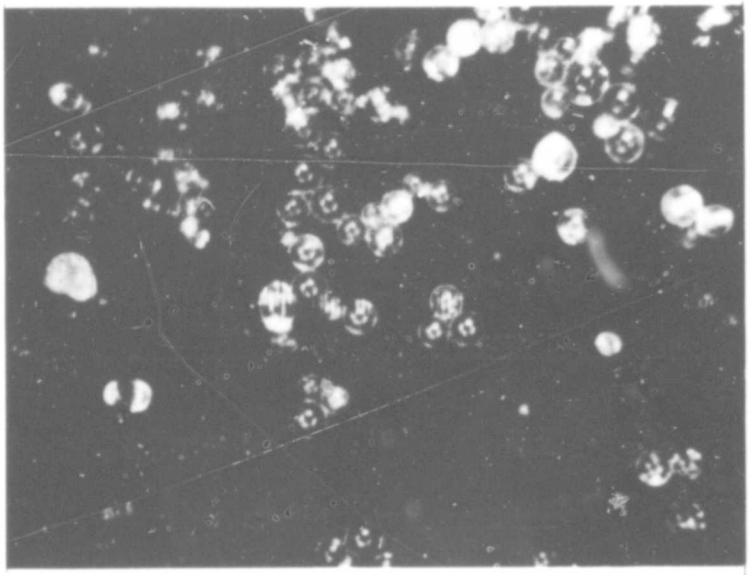

(a) 2.8 MILL GLASS BEADS

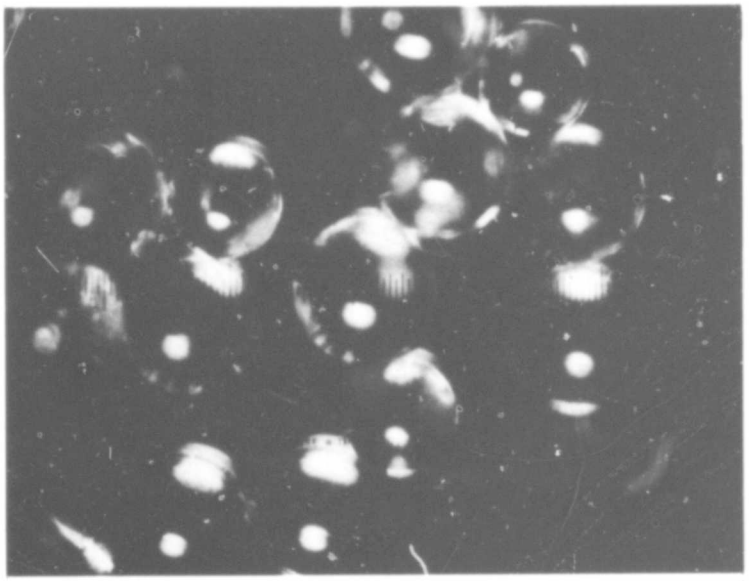

(b) 11 MIL GLASS BEADS

FIGURE 3 GLASS BEADS USED IN EROSION EXPERIMENTS (70X)

TABLE I

MECHANICAL PROPERTIES OF
FUSED SILICA AND SODA LIME GLASS

	Soda Lime Glass	Fused Silica
Density (lb./in.^{3})	0.0866	0.0795
Poisson's Ratio	0.22	0.17
Young's Modulus (lb/in^2)	10.0×10^6	10.68×10^6

TABLE II

EROSION TEST SCHEDULE

SPECIMEN	BEAD SIZE (MILS)	BEAD FLOW RATE (LB/MIN.)	IMPACT VELOCITY (FT./SEC)
G1	2.8	2	200
G2	11.4	1	200
G3	11.4	1	300

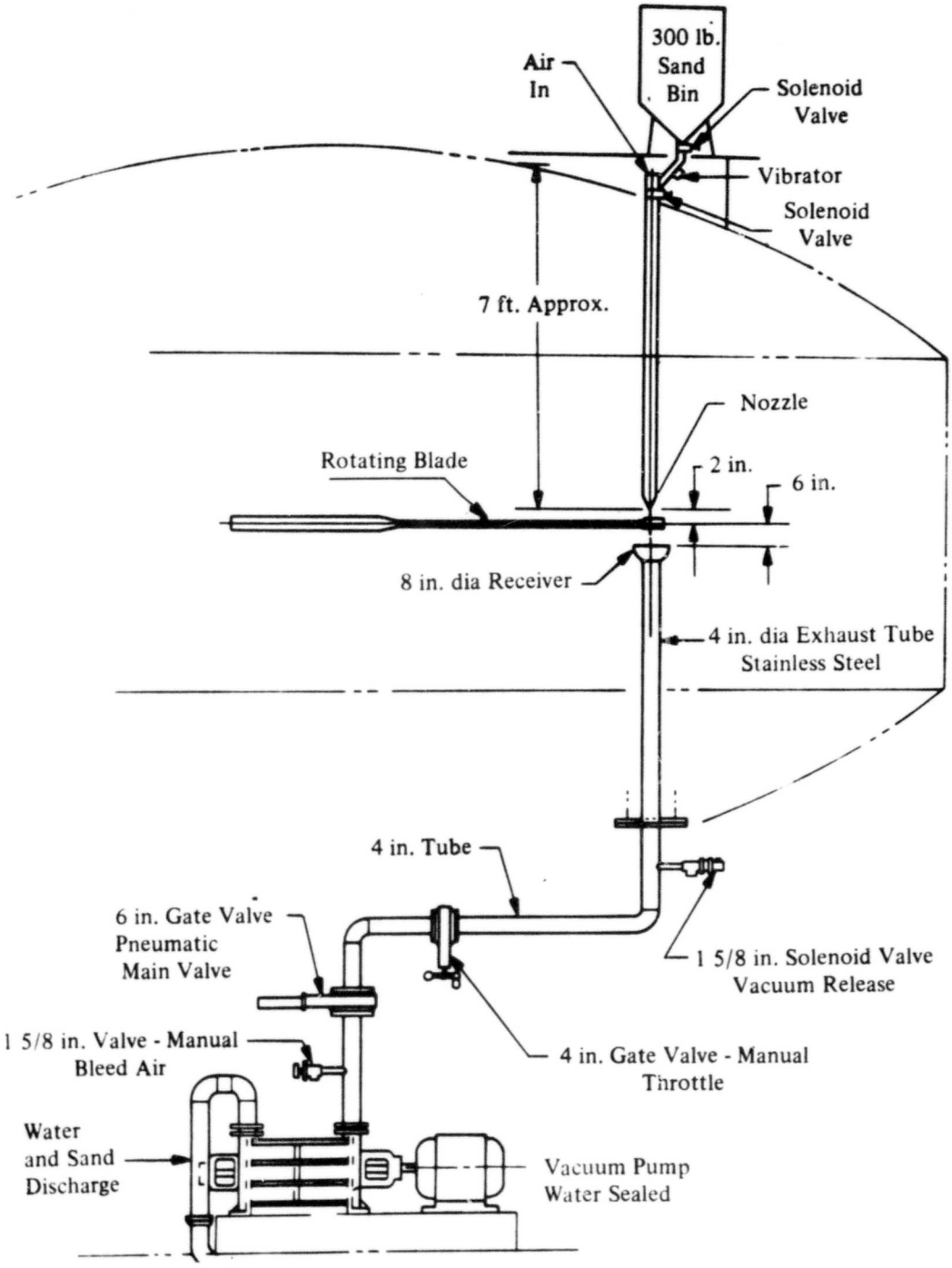

Figure 4. Sand Injection and Exhaust System
for AFML/Bell Erosion Apparatus

1 3/8 inch diameter blast tube which is approximately 7 feet long. They are dropped through the plane of the rotating arm from an elliptical nozzle which has a major axis of 1 7/8 inch and a minor axis of 7/8 inch. Due to the elliptical opening at the end of the drop tube the distribution of beads is nonuniform along the length of the specimen. Modification of the nozzle is under consideration to provide a uniform distribution of particles along the length of the specimen.

The rate of flow of the beads was calibrated by weighing the beads which fall from the tube for a number of settings on the feed mechanism. Although it was not possible to ascertain directly the actual number of beads striking the surface of the specimen, a theoretical calculation of the maximum number of impacts is possible.

Let N be the number of beads released from the hopper per second and x be the distance a bead falls from the feeder due to gravity at time t,

$$x = \frac{1}{2}gt^2 \tag{21}$$

The density of the stream of beads will vary along the length of the tube. At a distance x from the release point, the spatially-dependent density $\rho(x)$ is given by

$$\rho(x) = \lim_{\Delta t \to 0} \frac{N(t+\Delta t) - Nt}{A\ \Delta x} = \lim_{\Delta t \to 0} \frac{N}{A}\left(\frac{\Delta x}{\Delta t}\right)^{-1}$$

or

$$\rho(x) = \frac{N}{A}\frac{1}{\sqrt{2\,gx}} \tag{22}$$

using Eq. (21). A is the cross-sectional area of the stream of beads. The maximum number of impacts on the specimen per revolution of the rotating arm is

$$N_I = \left(\frac{\text{beads}}{\text{unit volume}}\right)\left(\frac{\text{volume intercepted}}{\text{revolution}}\right)$$

$$= \left(\frac{N}{A}\frac{1}{\sqrt{2gh}}\right)(Ad) = \frac{Nd}{\sqrt{2gh}} \tag{23}$$

where $x = h$ is the distance from the feeder to the plane of the rotating arm and d is the height of the specimens.

The number of 11 mil beads in 1 lb. was determined to be 1.5×10^7 beads. There are 10^9 2.8 mil beads in 1 lb. Thus for typical dimensions of $h = 7$ ft., $d = 0.0625$ ft., and a flow rate of 1 lb/min., $N_I = 49{,}000$ impacts/rev. (2.8 mil beads) and $N_I = 740$ impacts/rev. (11 mil beads).

The velocity, v, of the specimen near its midpoint on the rotating arm is related to the rotational speed of the arm, Ω, measured in revolutions per minute (RPM) by

$$\Omega = 1.06v$$

when v is measured in ft/sec.

The basic premise of the theory developed in Section III is that erosion occurs through preferential growth of eroding regions on the surface of the specimen. The pit nucleation function and mean growth rate are the statistical parameters which represent this process. A straight-forward procedure for obtaining explicit representations of these functions is the direct observation of nucleated erosion sites on the sample surface as a function of time. The greater the number of sites tabulated, the more accurate the statistical data will be. The experimental program is designed to evaluate the damage to the eroded surface of fused silica specimens after incremental exposures to the direct impact of spherical glass beads in the AFML-Bell erosion apparatus.

The specimens were handled with cotton gloves, weighed and carefully mounted in the specimen holder on the blade. They were exposed to the direct impacts of the glass beads for time periods which increased with the increase in the cummulative time of exposure. The damage process in each specimen was monitored microscopically after each time increment in order to evaluate the statistical parameters for the proposed theory and determine the erosion mechanisms responsible for the nucleation of pits in the eroding surface. The scale of the damage was such that optical microscopy could be used to make the necessary observations. A special staging plate was designed and fabricated for the Bausch and Lomb Metallograph which made it possible to return

consistently to within a few mils of a particular location on the surface of a specimen. A magnification of 110X was found to be adequate for observing the details of the erosion process which were seen best using dark field.

The experimental procedure for recording the extent of the erosion damage after each incremental exposure on the rotating arm was first to survey the entire surface for any unusual feature produced by the particle impacts. Then a total of seventy-five sites, approximately sixty mils in diameter located in the central region of the specimen are investigated in detail. In the initial stages of the erosion process the number of ring fractures is counted for each site along with the number of double, triple, and more complex ring fracture interactions. When possible, the observed damage was recorded photographically. The depth of a particular feature on the surface can be measured to within a few microns using the Metallograph. By setting the focus at a level below the surface, it is possible to note the extent of the damage at this level based on areas which are in focus as the surface of the specimen is scanned. It is, therefore, possible to divide the specimen into a number of layers using the optical microscope in conformity with the proposed model.

In order to minimize the effect of surface imperfections, three specimens of fused silica (G1 to G3) were prepared with highly-polished surfaces. Replicas were made of the surfaces and viewed in the transmission electron microscope at magnifications up to 38,000X. The highly-polished surfaces were featureless: no surface flaws could be detected and only rarely was an inclusion observed. As indicated in the literature [16], surface flaws cannot be observed in this way. Other means devised for the direct observations of flaw distributions in glass surfaces are still viewed with uncertainty as to the evaluation of the actual distribution and that which was induced by the experimental procedure used. In this initial study no detailed investigations were made of the flaw distributions on the original surfaces of the specimens, since the perfection of the highly-polished surfaces would be disrupted by the experimental procedures. When flaw distributions are required, test bars of fused silica which received the same treatment as the specimens are available for this evaluation either through direct or indirect means.

The equivalent static load, radius of contact area, and duration of impact can be calculated from the Hertz theory, Eq. (18), (13) and (19), using the velocities for the erosion test conditions specified in Table II and the mechanical properties in Table I. The results of these computations are listed in Table III.

TABLE III

HERTIZAN IMPACT PARAMETERS FOR FUSED SILICA

	Equivalent Static Load, P(lb.)	Radius of Contact Circle, a(in.)	Duration of Contact, T(sec)
2.8 Mil Glass Beads			
200 fps	0.215	0.350×10^{-3}	1.19×10^{-7}
300 fps	0.355	0.415×10^{-3}	1.10×10^{-7}
11 Mil Glass Beads			
200 fps	3.56	1.430×10^{-3}	4.76×10^{-7}
300 fps	5.88	1.692×10^{-3}	4.40×10^{-7}

The results in Table III show that the maximum contact area is large in comparison to the diameter of the impacting beads which cast some doubt on the satisfaction of the basic assumption of the Hertzian analysis. Assuming the Hertzian approach is valid, the calculated duration of contact (on the order of 10^{-7} seconds) indicates that a dilatational wave* will travel a maximum on 0.1 in. from the initial point of contact during this time interval. The shear and Rayleigh waves will have traveled only 0.06 inch. On the basis of these distances in relation to the dimensions of the maximum contact area and bead size, the quasistatic loading requirements for the treatment of impact phenomena can also be questioned. The impact conditions in the experimental program were dictated by the size of the sample which could be accommodated on the rotating arm. This placed a restriction on the size of the impacting particles.

*The speed of a dilatational wave in fused silica is 19,600 ft/sec at 70°F° and a shear wave travels at 12,350 ft/sec.

B. EROSION MECHANISMS IN FUSED SILICA

Although a variety of inorganic glasses have been used in erosion studies reported in the literature, no information could be found on the operative erosion mechanisms associated with the various stages of the weight-loss data for glasses subjected to multiple solid particle impacts. The erosion data for solid particles impacting brittle materials are generally reported in terms of plots of the mass of specimen loss per unit mass of eroding particles (or an equivalent measure of erosion) as a function of the particle impingement angles. Such an approach only provides the steady-state erosion rate for a prescribed particle size (or distribution of particle sizes), particle shape, and impact velocity. The work reported here investigates the erosion mechanisms in an inorganic glass when eroded by multiple collisions with relatively small particles.

Specimen G1 was exposed to impacts by 2.8 mil beads at 200 fps (or the equivalent of 212 RPM on the rotating arm). The bead flow rate was 2 lb/min., so according to Eq. (23) the maximum number of bead impacts should be on the order of 98,000 impacts/rev. The specimen had a cummulative exposure time of 72 minutes.

The erosion test for specimen G1 was exploratory. During the early stages of erosion, under 8 min., the eroded

surface was composed of a distribution of ring fractures, small pitted areas less than 1 mil in diameter, and a distribution of very small imprints, less than 0.1 mil, due to collisions which did not produce measurable damage. The average diameter of the ring fractures was 3 mils with very little deviation from this value. The formation of these rings on the surface and their interaction was assumed to be the primary mechanism of material removal. A portion of the ring fractures are accompanied by material removal just outside the ring perimeter: the interior of the circular ring is undisturbed. Larger-scale material removal occurs in the interstitial areas of non-overlapping double and triple ring fractures. A limited number of more complex forms of ring intersections are beginning to develop at this time.

The volume removed from the interstitial region between ring fractures was considered to be the nucleation site for a pit on the surface. The location of these sites in the central region of the specimen were recorded. The larger pits nucleated were re-examined after subsequent incremental exposures to the eroding environment, and it was found that none of the previously established pits showed any growth. The density of 3 mil ring fractures on the surface of the fused silica as a function of exposure time is a significant factor in the continual growth of pitted regions as defined above. The graph in Figure 5 shows that the ring density (evaluated for the central region of

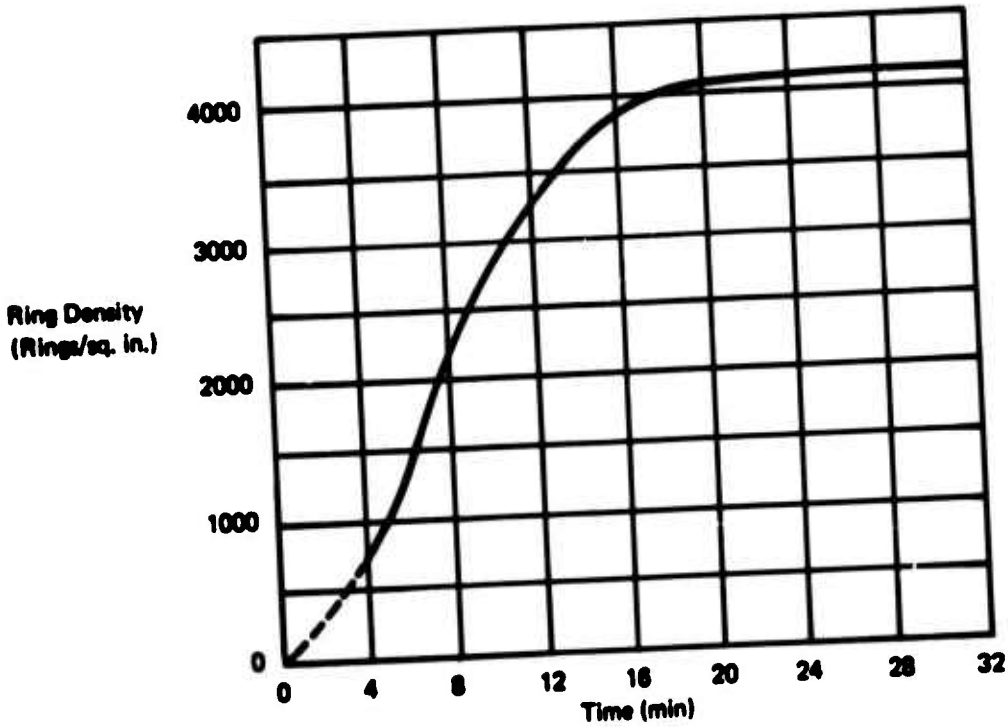

Figure 5. Variation of the Density of 3 mil Fracture Rings on the Surface of Specimen G1 as a Function of Exposure Time

the specimen) reaches a constant value after an exposure time of 24 minutes. This was a somewhat unexpected result. On the basis of the number of impacts per revolution, the specimen will have collided with 1.66×10^8 beads after 8 min. and three times this number at 24 minutes. This makes the probability for a 3-mil ring fracture to occur quite low. After an exposure time of 32 min. the microscopic observations made it quite clear that the interaction between the 3-mil rings was not the primary erosion mechanism, but that fine-scale chipping of the surface was the dominant erosion mechanism.

The series of micrographs in Figure 6 illustrate the time evolution of the erosion process in the vicinity of a grouping of 3 mil ring fractures. At 8 minutes a number of ring fractures have interacted to remove a portion of the interstitial material. The faint outline of a number of isolated ring fractures can also be seen in the general area of this flaw. It was of interest to see if subsequent impacts in the vicinity of this nucleated site would extend the area of the material removed in accordance with the proposed model. The micrograph of the same region at 16 minutes shows evidence of a large number of particle impacts, but essentially no new ring fractures result. Instead, the solid particle collisions are restricted to fine-scale chipping which is clearly seen to be preferential in the vicinity of the existing ring fractures. Some of the ring fractures which are

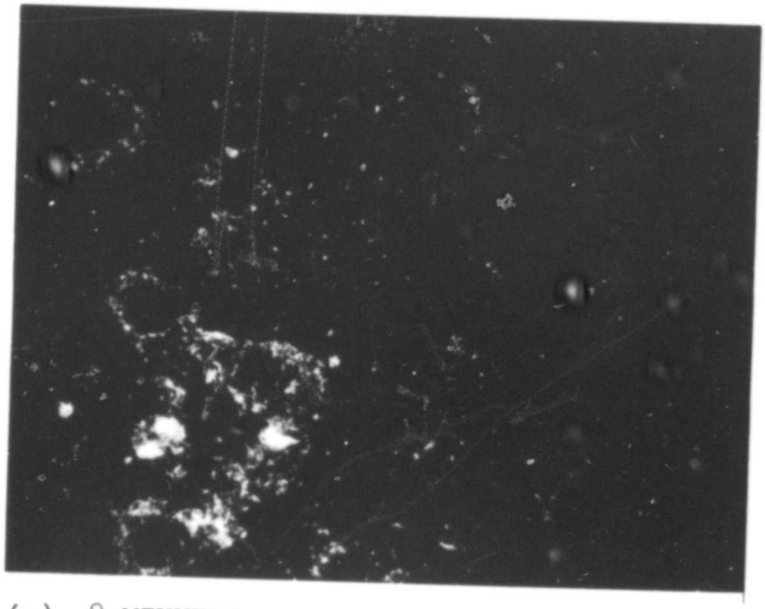

(a) 8 MINUTES

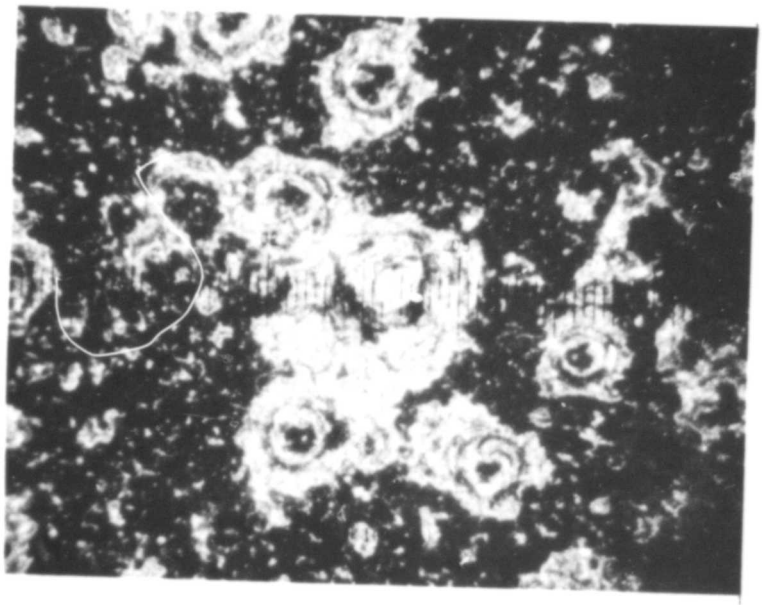

(b) 16 MINUTES

FIGURE 6 EROSION IN THE VICINITY OF 3-MIL RING FRACTURES ON SPECIMEN G1 (110X).

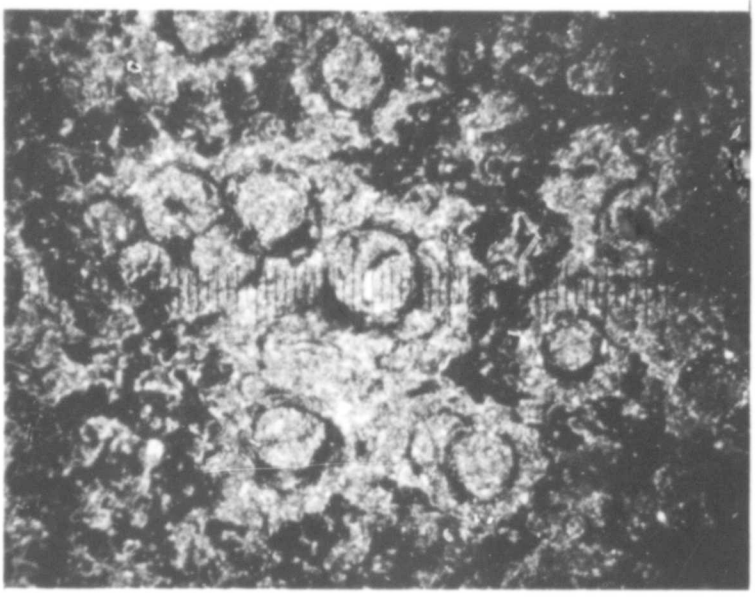

(c) 32 MINUTES

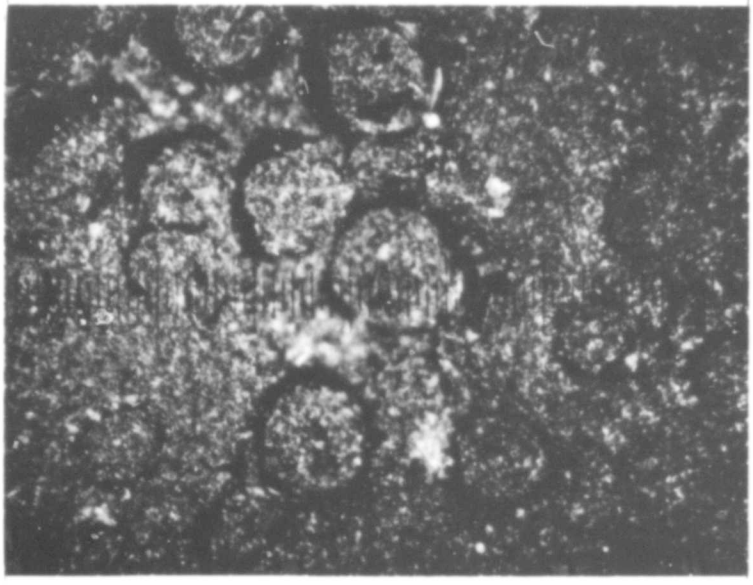

(d) 56 MINUTES

FIGURE 6 EROSION IN THE VICINITY OF 3-MIL RING FRACTURES ON SPECIMEN G1 (110 X).

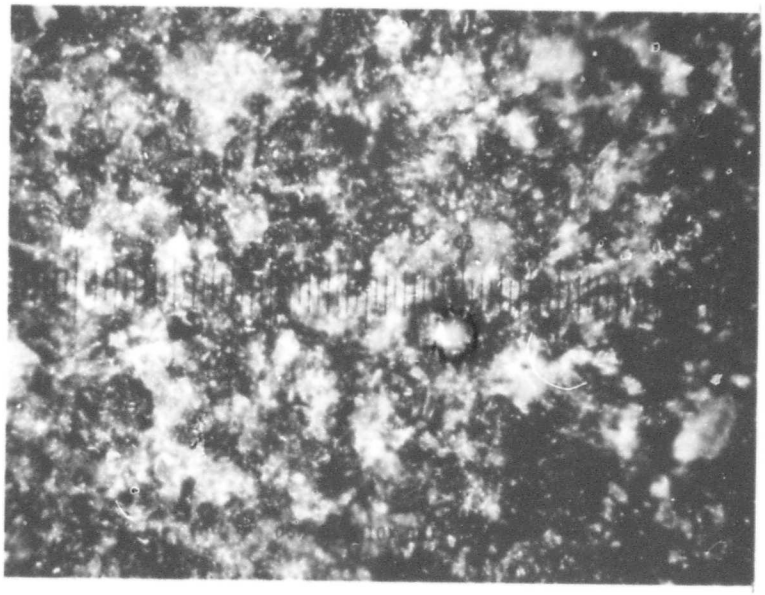

(e) 72 MINUTES

FIGURE 6 EROSION IN THE VICINITY OF 3-MIL RING FRACTURES ON SPECIMEN G1 (110X).

very faint in Figure 6a are now well-decorated. As the exposure time increases very small pieces are preferentially removed from the regions of initial damage. The original interstitial region between ring fractures exhibits no growth by subsequent ring fracture interactions. Material is continually removed by chipping of material from the periphery and within the eroded regions. This process continues until the original surface of the sample is completely removed as shown in Figure 6d. After 72 minutes the initial features of the impacted surface can no longer be identified.

Another sequence of micrographs is provided in Figure 7 which shows a triplet of interacting ring fractures where the conical portion of one ring has been removed by crushing. This region was first observed at an exposure time of 16 minutes. The volume of material removed is 6 mils by 6 mils and 40 microns deep. There was no change in the configuration at 24 minutes except that the fine-scale chipping has been active and is beginning to decorate the ring fractures already present. The micrograph of the same area at 32 minutes indicates that no new ring fractures have been formed in this region. The micrograph in Figure 7 shows that there is a lot of loose material which can be removed easily on subsequent impacts. It is at this stage that the rate of material removal should be uniform and proportional to the number of impacting particles.

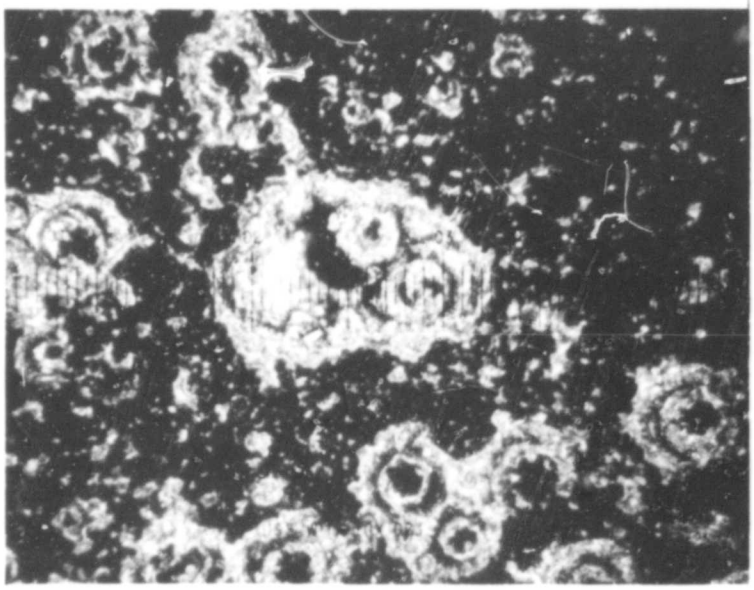

(a) 24 MINUTES

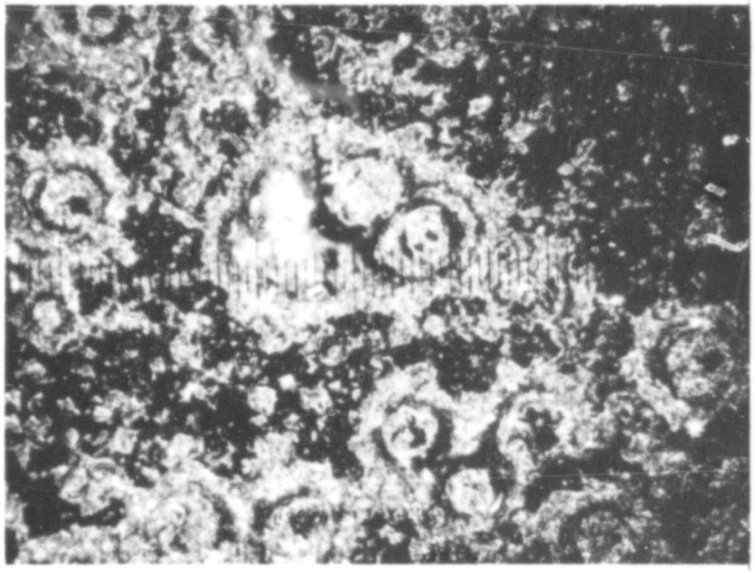

(b) 32 MINUTES

FIGURE 7 EROSION IN THE VICINITY OF A LARGE 6 MIL PIT ON SPECIMEN G1 (110X)

(c) 40 MINUTES

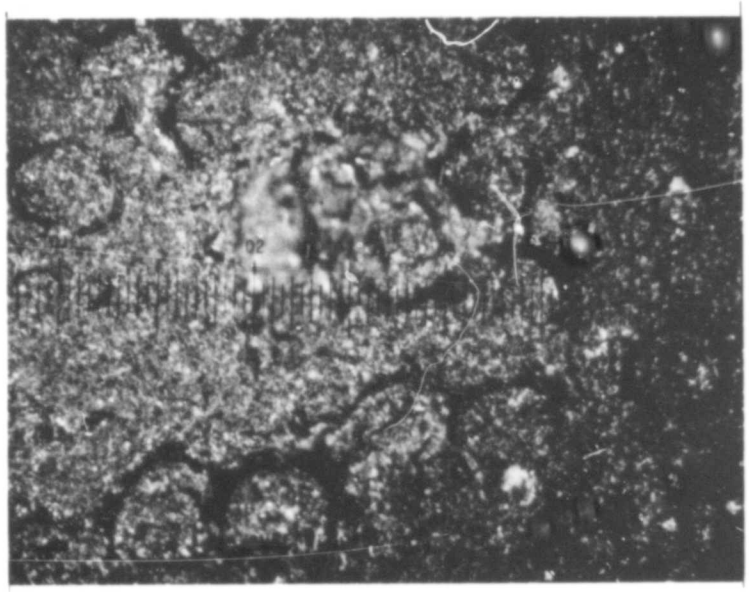

(d) 56 MINUTES

FIGURE 7 EROSION IN THE VICINITY OF A LARGE 6-MIL PIT ON SPECIMEN G1 (110X)

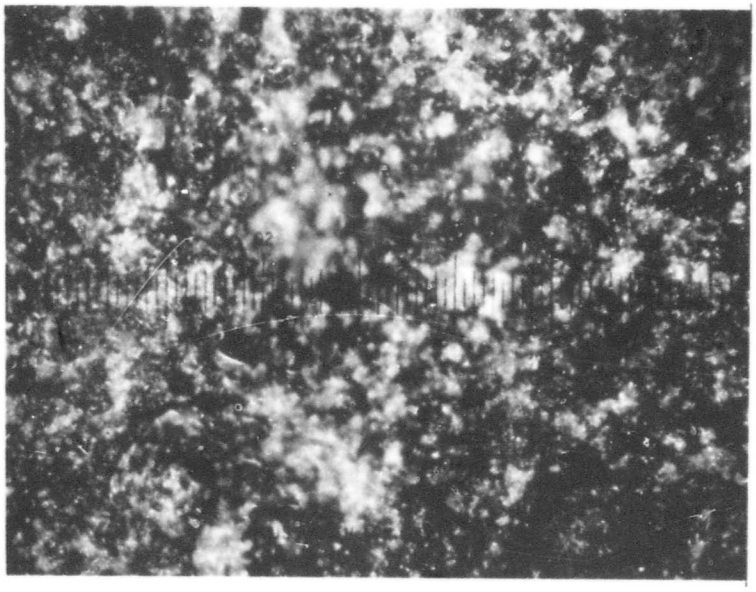

(e) 72 MINUTES

FIGURE 7 EROSION IN THE VICINITY OF A LARGE 6 MIL PIT ON SPECIMEN G1 (110X)

An example of a spalled region is shown in Figure 8. Larger areas, approximately 10 mils in diameter, were occasionally removed from the surface in the early stages of the erosion process, however this was not considered a major contributor to the overall weight loss. There is no evidence of large-scale growth at this nucleation site, but a fine-scale chipping away of the material within the original pit and in the surrounding region. The angularity of the cleaved surfaces is nearly eliminated after an additional exposure of 24 minutes.

The observations made with respect to Figures 6 to 8 are universal and are applicable to all of the large-scale areas of material removal. The removal of the interstitial material between adjacent ring fractures is negligible and is no longer an operative mechanism once the relatively short exposure time is reached associated with a stabilization of the ring fracture population. No large-scale growth was observed at any of the nucleation sites where measurable material removal took place by ring fractures or spallation. The original conjecture as to the principal erosion mechanism in fused silica using 2.8 mil glass beads was shown to be incorrect. The initiation and continuation of the erosion process is due entirely to the fine-scale chipping associated with the 2.8 mil beads.

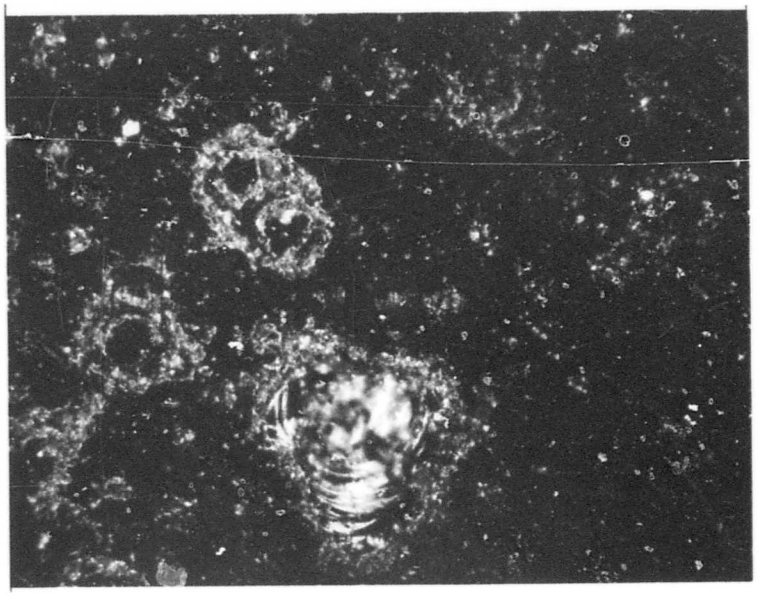

(a) 32 MINUTES

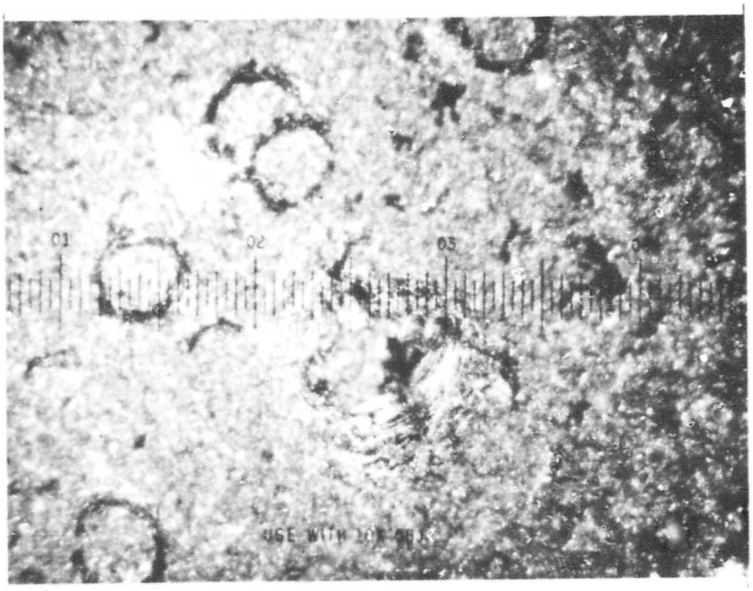

(b) 56 MINUTES

FIGURE 8 EROSION IN THE VICINITY OF A SPALLED REGION ON SPECIMEN G1 (110X)

The fine-scale chipping process can be seen to be preferential and until the time the original surface has been removed, somewhat dependent on the distribution of 3 mil ring fractures on the surface. Definite growth of the nucleated areas can be seen in Figures 6 and 7. This process is in accordance with the proposed statistical model. However there are certain limitations which make it extremely difficult to evaluate the data required in the proposed theory using direct microscopic observation of the eroded surface. It is believed that these difficulties can be overcome in the future.

Closer examination was made of the damage associated with what has been referred to as fine-scale chipping. At higher magnification, 280X, it was seen that the small pits in the range of slightly less than 0.1 mil to approximately 1 mil were in essence material removal on the periphery of incomplete ring fractures whose average diameter was 0.9 mils. Complete ring fractures were also found, but usually only a portion of the material along the circumference is removed. These fractures were single rings, so the force imparted by the particles to the surface must have been just sufficient to create the ring fractures. The general character of the damage on this scale is shown in Figure 9. The figure shows the neighborhood of the 3-mil rings and interactions of the small rings. The rings are formed perferentially and seem to congregate in the neighborhood of existing rings. The

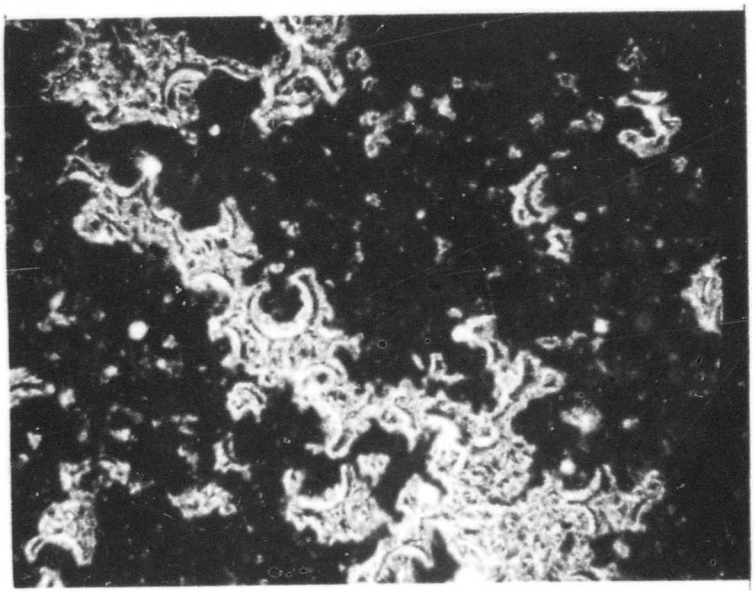

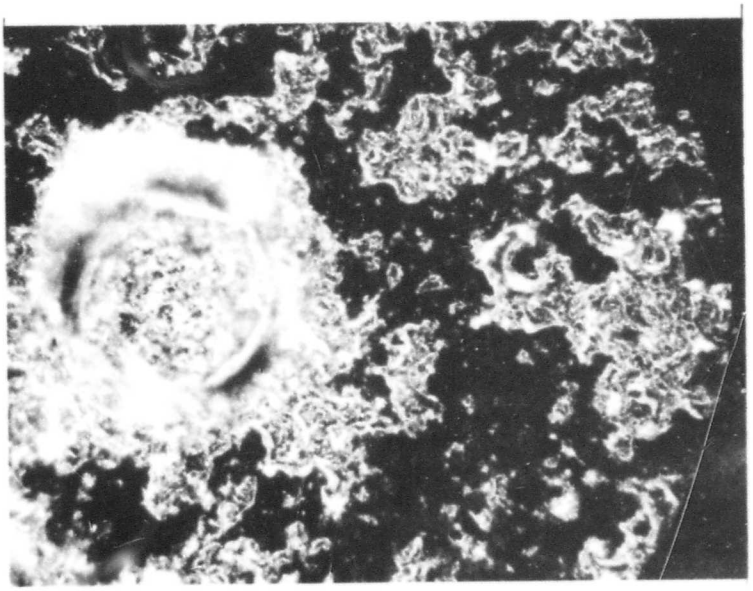

FIGURE 9 0.9 MIL RING FRACTURES ON THE SURFACE OF SPECIMEN G1 (280X)

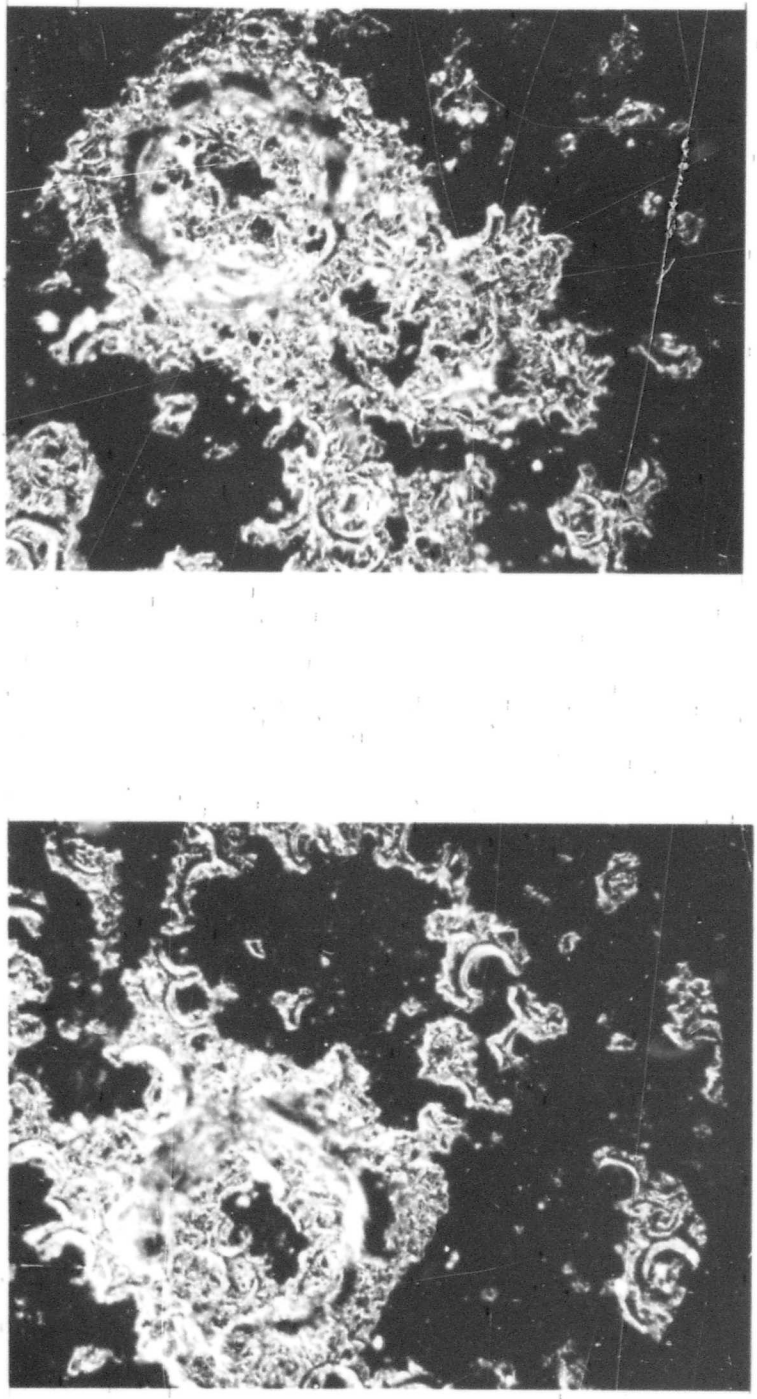

FIGURE 9 0.9 MIL RING FRACTURES ON THE SURFACE OF SPECIMEN G1 (280X)

depth of the materials removed is only 5 to 10 microns per impact. It was not possible to count all of the pits of this type or to record their locations and dimensions. The manner of growth is by ring fracture intersections, but alternative methods will have to be devised for evaluating the area removed as a function of time.

The weight-loss data for specimen G1 is given in Figure 10. After an exposure time of 70 minutes the rate of material removal is reaching a steady-state level. It can also be seen that only 3 mg is removed from the surface at the exposure time when the probability for the occurrence of a 3 mil ring is zero (Figure 5). This provides further support for the conclusion that the 3 mil ring fractures have an insignificant role in the overall erosion process.

Specimen G2 was exposed to the 11 mil glass beads at a velocity of 200 fps and a bead flow rate of 0.0167 lb/sec. The sample will experience a maximum of 740 particle impacts per revolution of the rotating arm according to Eq. (22). The arm rotates at 212 RPM to attain a linear velocity of 200 fps at the center of the specimen. Specimen G3 was impacted by the 11 mil beads at 300 fps (or 318 RPM) at the same bead flow rate of 0.0167 lb/sec. The erosion process will be described for both specimens since the erosion mechanisms were the same differing only in the quantitative aspects of the process.

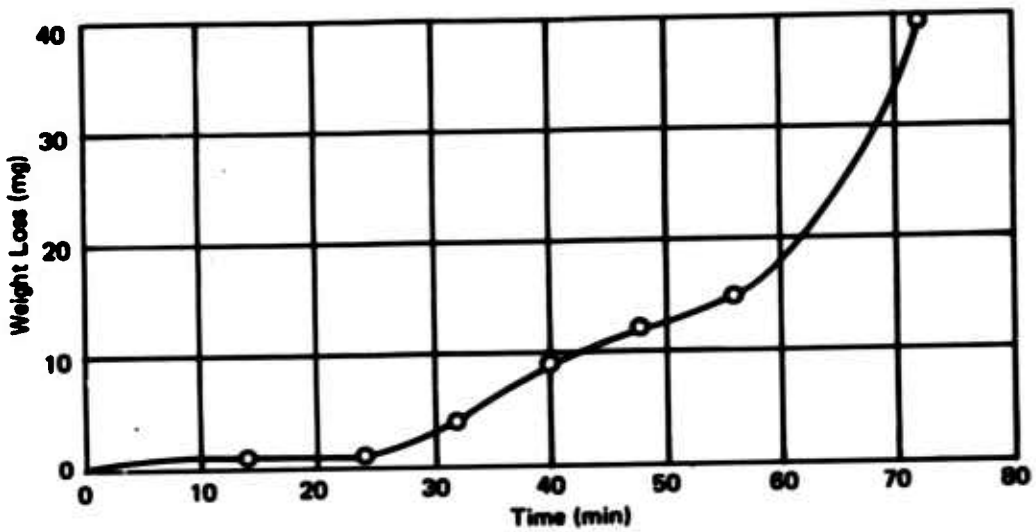

Figure 10. Weight - Loss Data for Specimen G1

The erosion process was greatly accelerated when the 11 mil beads replaced the 2.8 mil beads as evidenced in the weight-loss data in Figures 11 and 12. Although the weight-loss data are based on only one test, the characteristic shape can be correlated with the erosion mechanisms which will be described in a chronological manner. The erosion mechanisms operative before reaching the uniform erosion rates indicated in the weight-loss data are quite distinct from the fine-scale chipping mechanism associated with the 2.8 mil beads. The erosion mechanisms in the early stages of the erosion process using 11 mil beads are associated primarily with conical ring fractures and subsequent impacts on the damaged surface.

In order to observe a relatively low density of ring fractures on the surface of each specimen, they were exposed to the eroding environment for a time increment of approximately one second. Surface replicas were taken, and the surfaces were observed optically using Nomarsky phase interference. The optical micrographs, Figures 13 and 14, show that the central region of the inner ring is not damaged by the impacts. The circularity of the ring fractures indicates that normal impacts are taking place. It was not possible to see the cone fractures extending into the interior of the specimens at this point; however, subsurface interactions between the transient stress fields produced by particles impacting in the vicinity of already

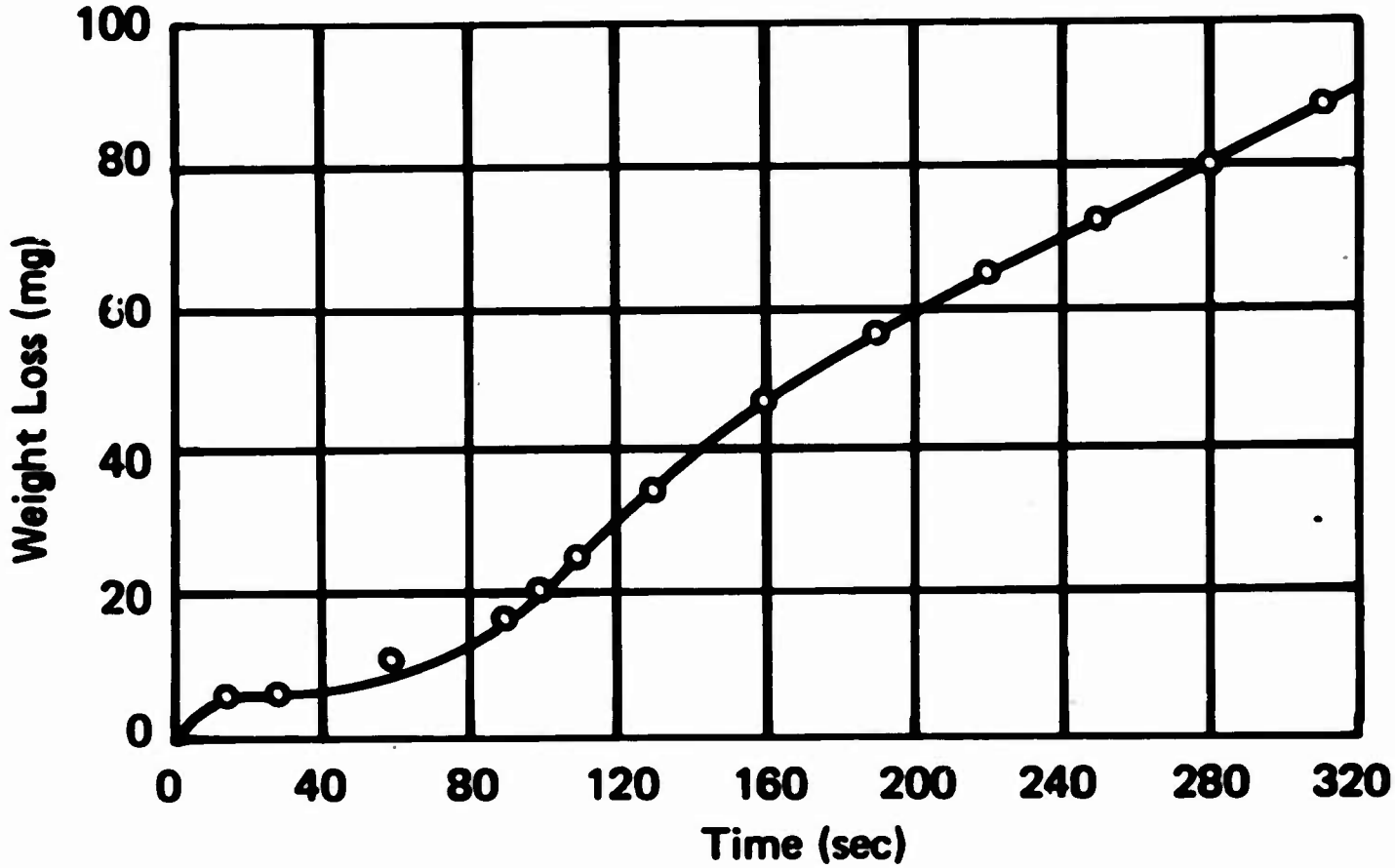

Figure 11. Weight-Loss Data
for Specimen G2

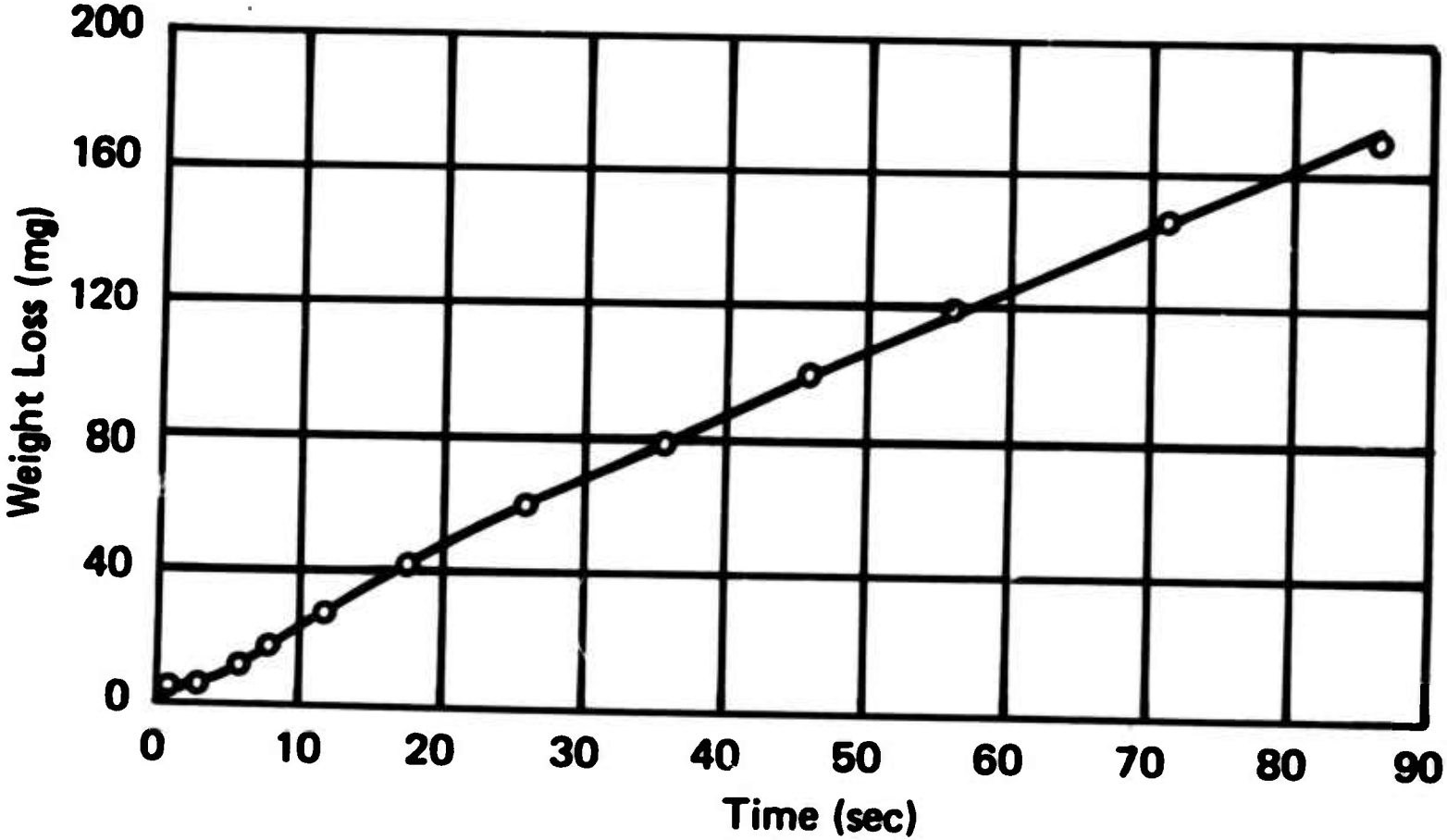

Figure 12. Weight-Loss Data
for Specimen G3

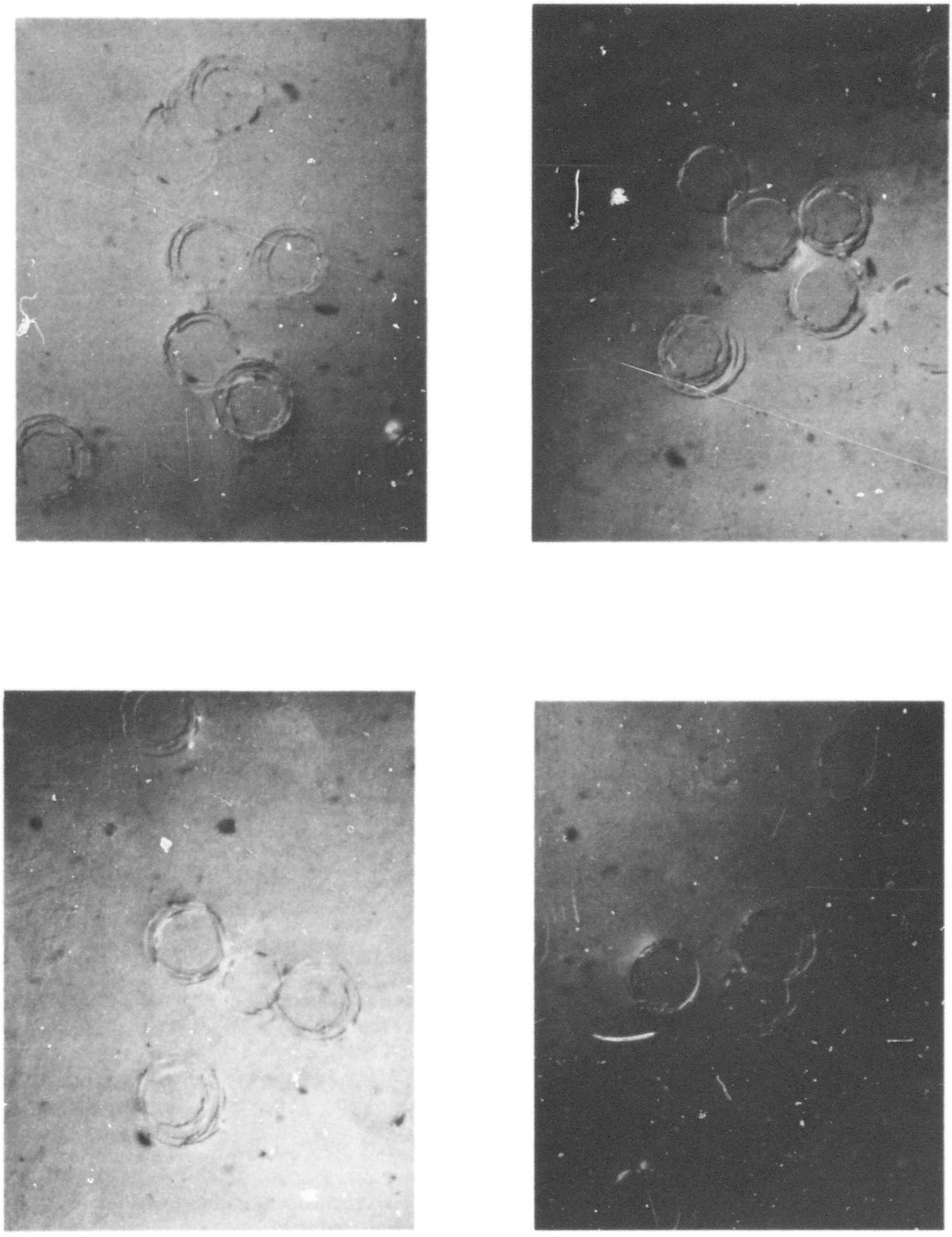

FIGURE 13 RING FRACTURES ON THE SURFACE OF SPECIMEN G2 AFTER IMPACT BY 11 MIL BEADS FOR 1 SEC. (125X)

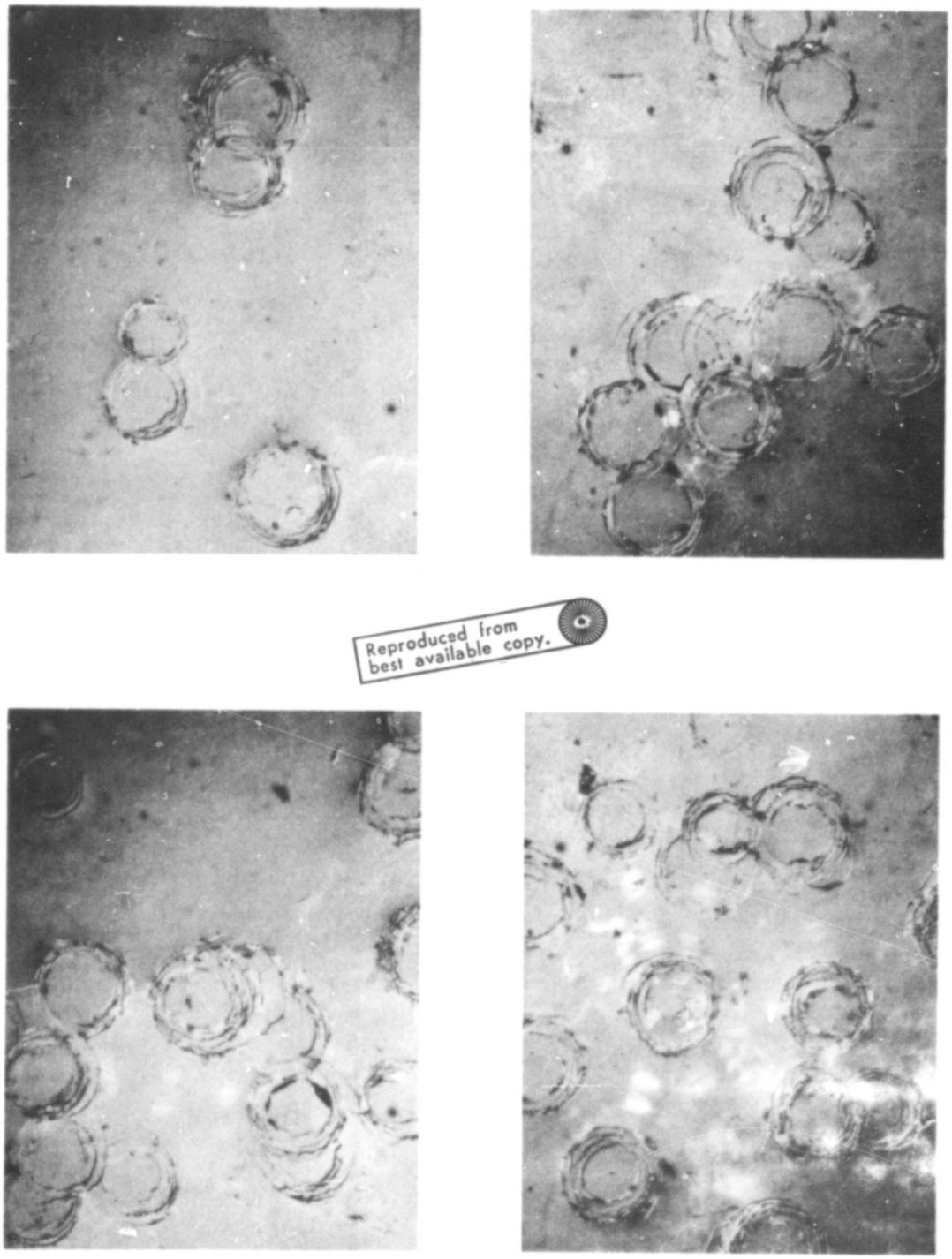

FIGURE 14 RING FRACTURE ON THE SURFACE OF SPECIMEN G3 AFTER IMPACT WITH 11 MIL BEADS FOR 1 SEC. (125X)

existing fracture surfaces could be observed by the reflection of light from these surfaces. A good example of this effect is seen in Figure 14, where a number of interactions have taken place. The ring fractures at 300 fps have outer rings which are approximately 30 percent larger than the outer rings for the ring fractures at 200 fps. The average diameter of the inner rings for the fractures formed at 200 fps and 300 fps is approximately 2.5 mils; however, the range of the inner ring sizes at 300 fps is fairly broad (1.8 to 3.3 mils), whereas the range of inner ring sizes at 200 fps is relatively narrow. According to Hertz theory, Table III, the diameter of the contact area should be 2.86 mils at 200 fps and 3.28 mils at 300 fps. The diameter of the outer rings in each case are greater than the calculated values for the contact area. The Hertzian predictions are in the range of the experimentally-determined ring fracture diameters.

Transmission electron micrographs of the ring fractures formed in the early stages of the erosion process are shown in Figures 15 to 18. Since the stress components are symmetrical about the contact area, the initial cracks will tend to be arcs of circles. However, the relaxation brought about by these fractures will produce a redistribution of stress with the tendency for the crack to propagate in a direction perpendicular to local trajectories of the maximum tensile stress. If the loading is continued, circular fractures will be produced at other flaws in the same manner as these initial cracks. According to Andrews[19], if the crack is able to follow the maximum stress,

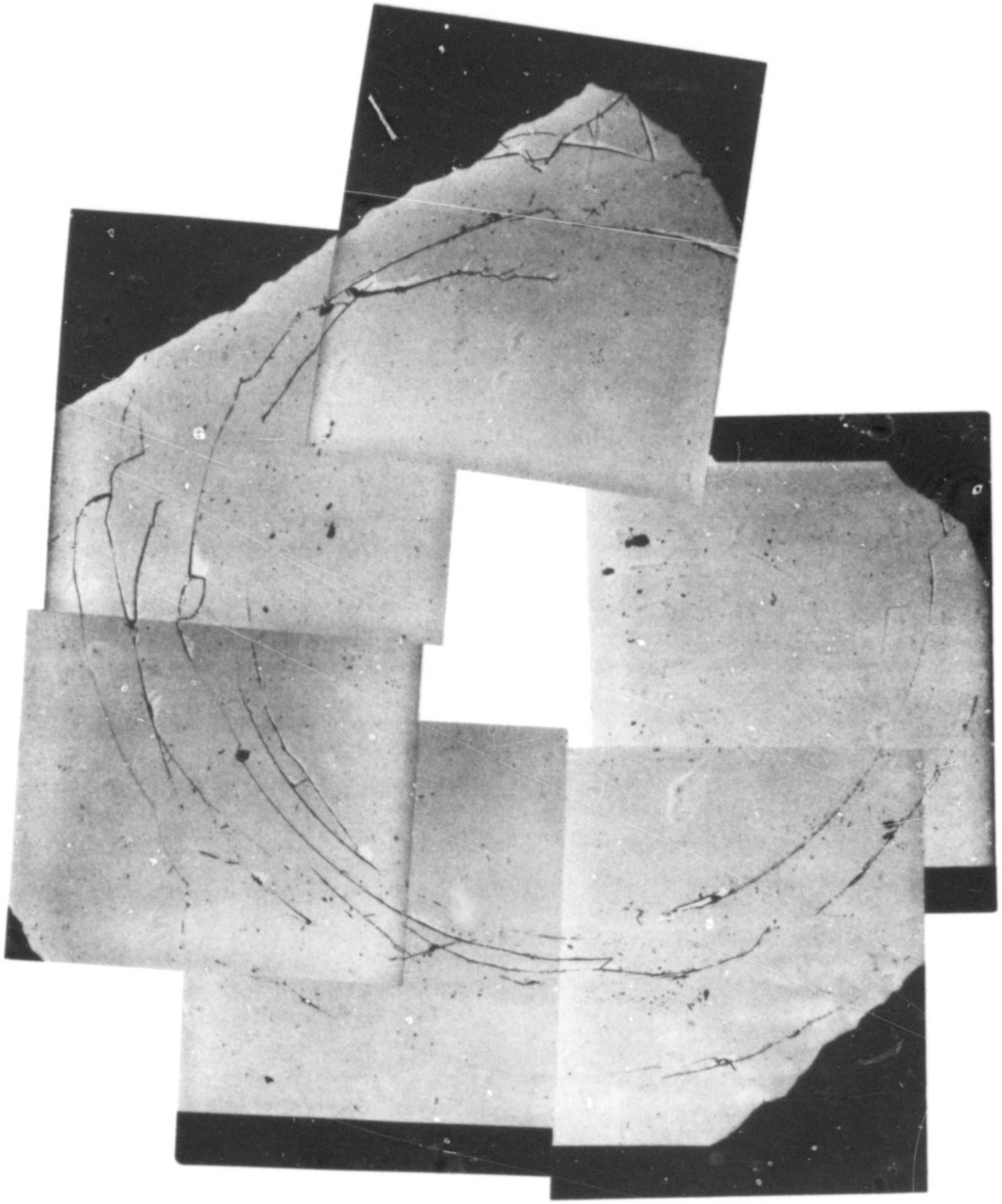

FIGURE 15 RING FRACTURE ON SPECIMEN G2 AFTER AN EXPOSURE TIME OF 1 SECOND (2000X)

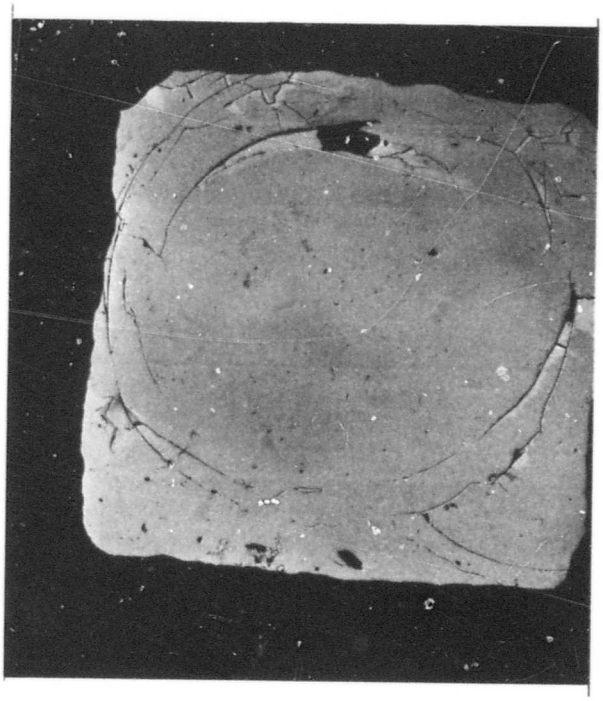

FIGURE 16 RING FRACTURE ON SPECIMEN G2 AFTER 15 SECONDS EXPOSURE TIME (1000X)

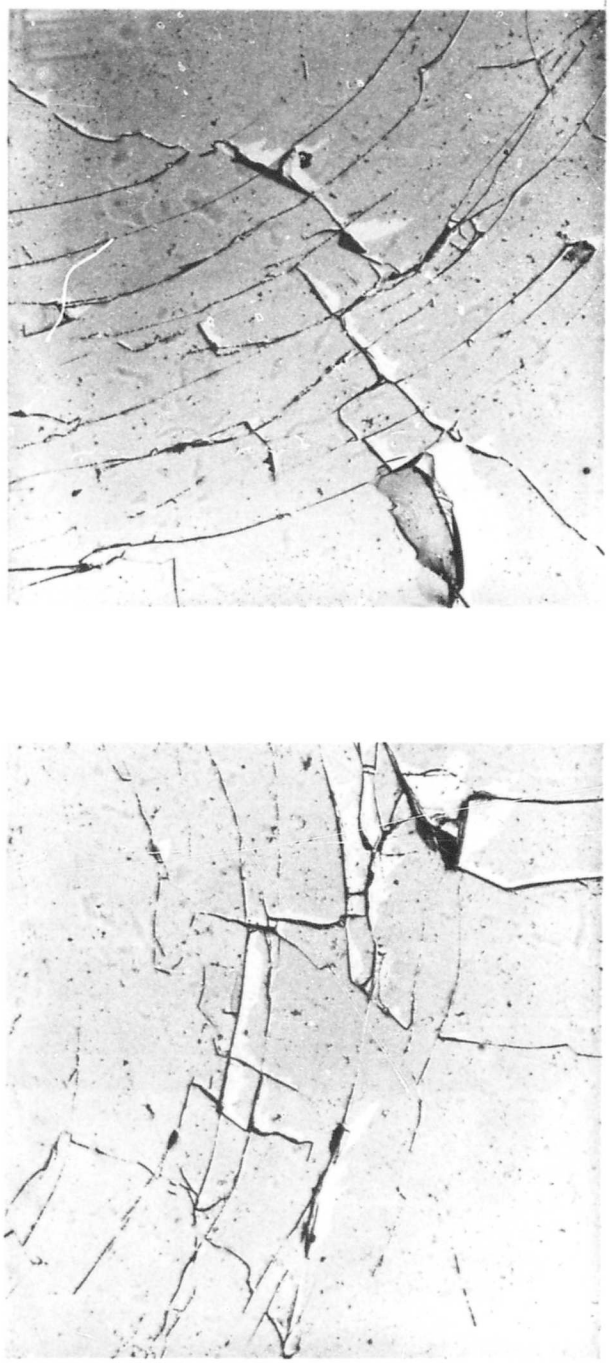

FIGURE 17 DETAILS OF RING FRACTURES ON SPECIMEN G3 AFTER AN EXPOSURE TIME OF 1 SECOND (2000X)

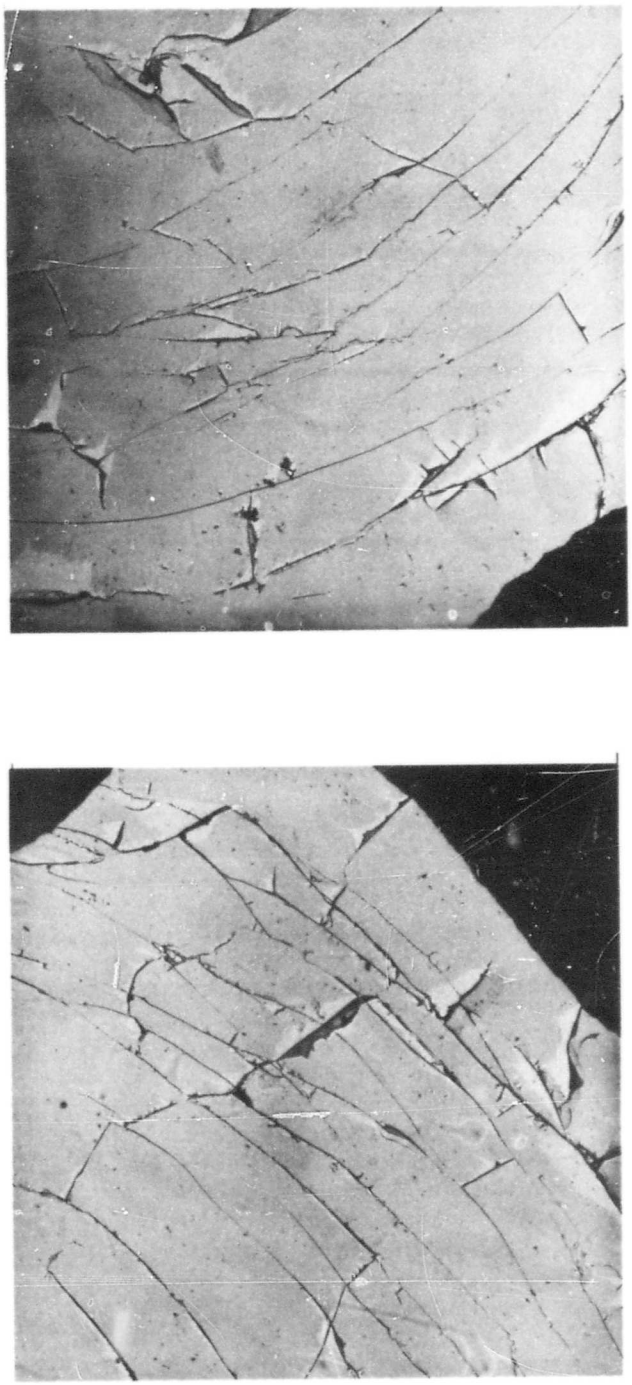

FIGURE 18 DETAILS OF RING FRACTURES ON SPECIMEN G3 AFTER AN EXPOSURE TIME OF 3 SECONDS (2000X)

it will not be circular. If, however, for any reason it is prevented from doing so, it may follow a more clearly circular outline for a short time and then branch off so as to bridge the distance between its present position and that of another circular crack. If fracture has begun at several places, development of each crack in this manner is to be expected giving rise to the complicated figures found in practice. The micrographs in Figures 15 to 18 are indicative of this process. Outside of this general observation, no particular characteristic of the ring fractures investigated using the electron microscope has been identified.

The observations of the specimen surfaces using Nomarsky phase interference and surface replication do not provide information pertaining to the characteristic subsurface conical fracture. The extent of the conical fracture surfaces extending into the interior of the specimen could not be seen around isolated ring fractures occurring in the very early stages of the erosion process. The features of the subsurface fracture surface did become evident when a second ring fracture occurred in the vicinity of an existing one. Figure 19 shows two ring fractures separated by a distance of 11-12 mils with no obvious stress wave interaction between them. Interactions between the dynamic stress field of an impacting particle which results in a new cone fracture and the flawed surface of a pre-existing ring

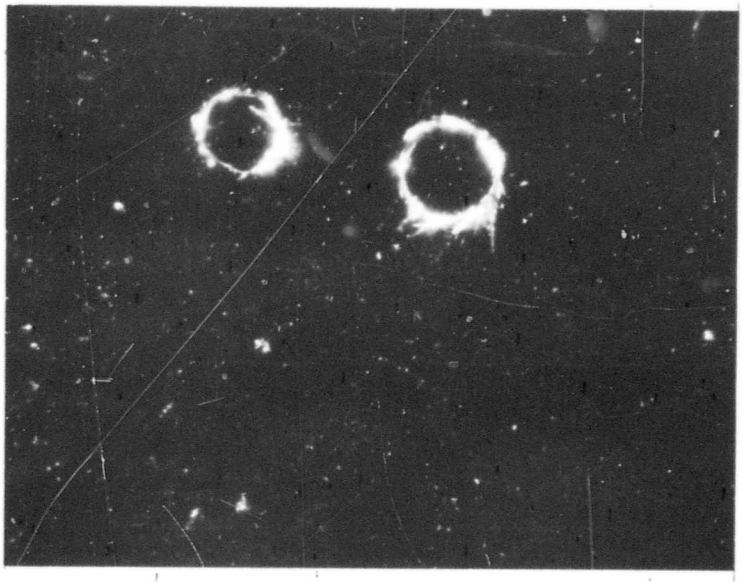

(a) NO INTERACTION BETWEEN FRACTURE SURFACES

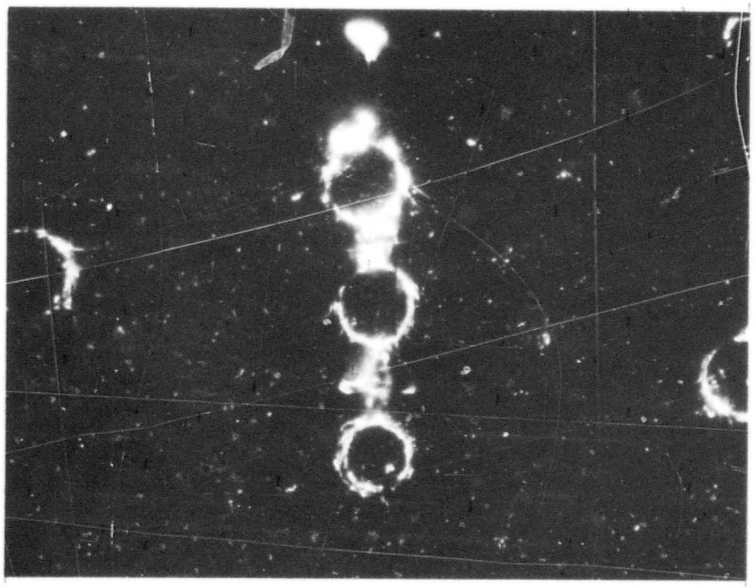

(b) INTERACTING SUBSURFACE FRACTURES

FIGURE 19 RING FRACTURES IN PYREX IMPACTED BY 11 MIL GLASS BEADS AT 300 fps (110X)

fracture were rarely found at separation distances greater than 12 mils. On the other hand, Figure 19b shows ring fractures produced under the same conditions separated by approximately 8 mils with a segment of the common fracture surface clearly visible. This effect was seen repeatedly in the microscopic observations. In nonoverlapping rings the interaction generally produced a short cracked boundary representing the intersection of the conical fracture surface associated with each ring fracture. This clearly visible demarcation is perpendicular to the line between the centers of the two adjacent ring fractures. A particle impacting just outside the periphery of a ring fracture produces a slightly different effect as shown in Figure 20. Overlapping ring fractures show surprisingly little influence on each other as seen in the Nomarsky interference micrographs, Figures 13 and 14, and in Figure 20. As more particles impact the neighborhood of the pre-existing ring fractures a complex pattern of subsurface fractures develop as shown in Figure 21. The micrograph in Figure 22a is taken at the surface of the specimen while the micrograph in Figure 22b is focused at a point below the surface which shows the straight-line segments produced in the manner described above. The subsurface fracture process continues without any significant material removal from the surface. Subsequent impacts on the interstitial regions between cone fractures produce an increasingly complex network of fracture surfaces, but no new cone fractures are produced in the highly-flawed interstitial areas. The general appearance of the surface

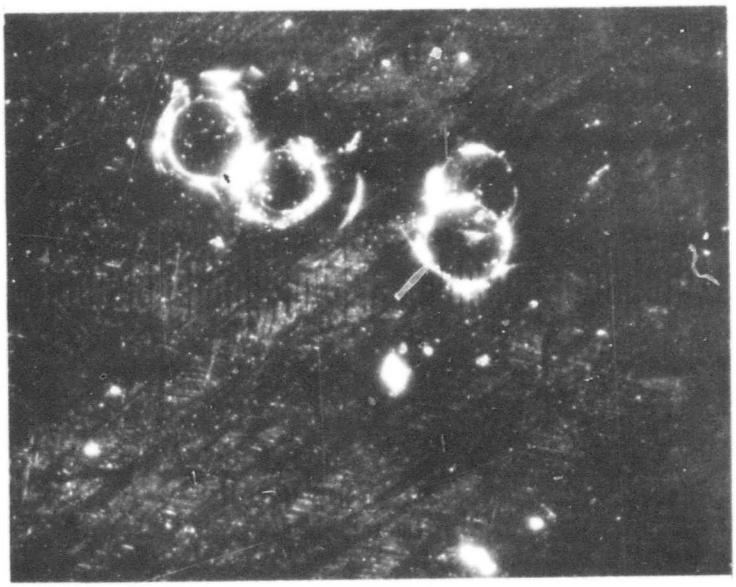

FIGURE 20 OVERLAPPLING AND NEARLY OVERLAPPING RINGS FRACTURE IN PYREX IMPACTED BY 11 MIL BEADS AT 400 fps (110X)

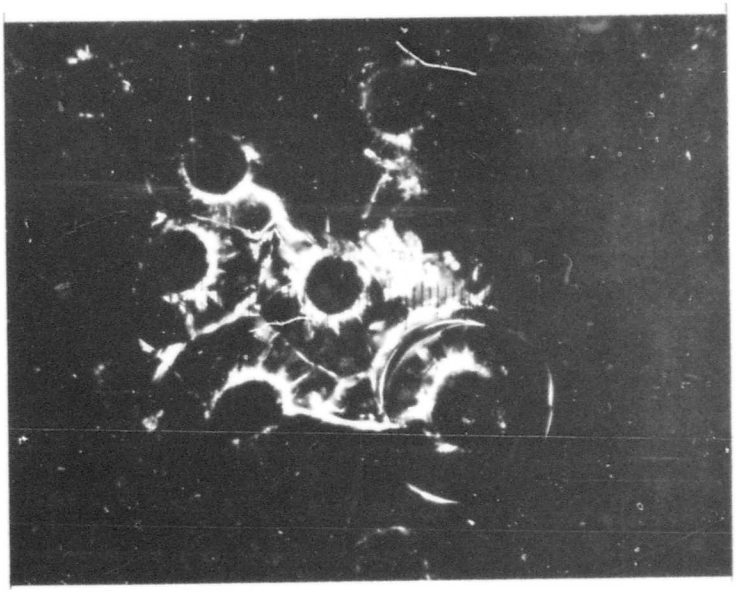

FIGURE 21 SUBSURFACE FRACTURE INTERACTIONS IN PYREX IMPACTED BY 11 MIL BEADS AT 400 fps (90X)

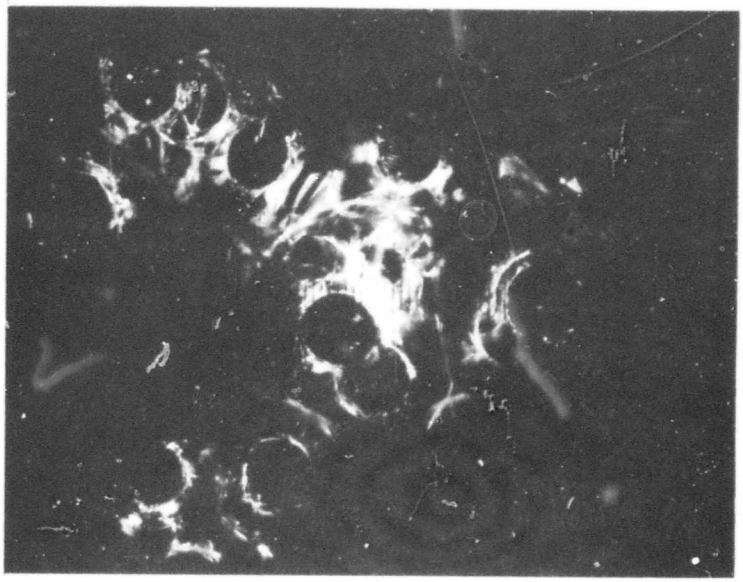

(a) FOCUSED AT SURFACE

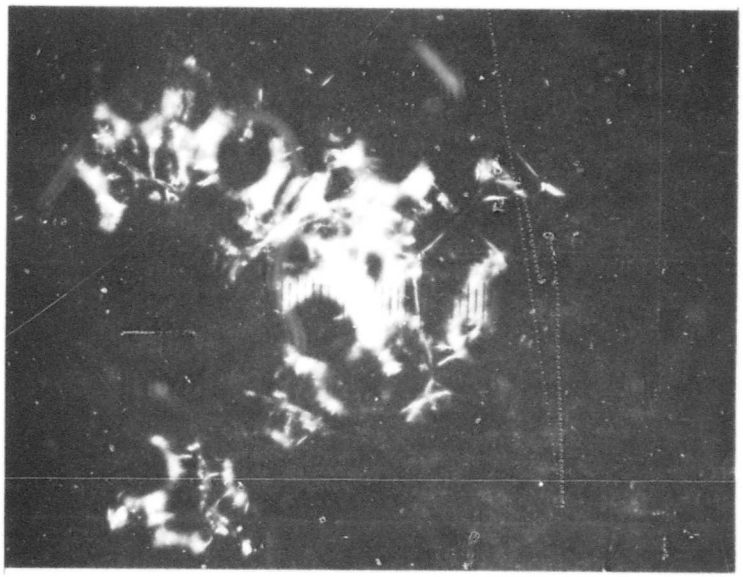

(b) FOCUSED BELOW SURFACE SHOWING FRACTURE SURFACE INTERSECTIONS

FIGURE 22 SUBSURFACE FRACTURE INTERACTION IN PYREX IMPACTED BY 11 MIL BEADS AT 400 fps (90X)

of specimen G2 at 15 seconds and 60 seconds is indicated in Figure 23. The small white spots on the micrograph are evidence of collisions which did not result in ring fractures. The particle bombardment has relatively little influence on the interior surface region of the ring fractures. The interstitial regions after an exposure time of 60 seconds are still intact over most of the surface area of the specimens.

The distribution of diameters of the inner rings of the ring fracture produced in specimens G2 and G3 is shown in Figures 24 and 25, respectively. These data were obtained at an intermediate stage of the overall exposure for each specimen and are based on measurements of 200 rings on the surface of each specimen. The average diameter for the inner rings for specimen G2 is 2.63 mils, while it is 2.51 mils for specimen G3. This result is consistent with the average diameter of the inner rings evaluated in the very early stage of the erosion process. The reason for the average ring size being larger at the lower impact velocity is believed to be due to measuring errors.

Surveying the central region of specimen G2, it was found that the density of ring fractures per square inch was 3336 at 15 seconds, 4140 at 60 seconds and 2930 at 130 seconds. Similar data for specimen G3 show that the ring fracture density (rings/square inch) is 1820 at 3 seconds and 1960 at 18 seconds

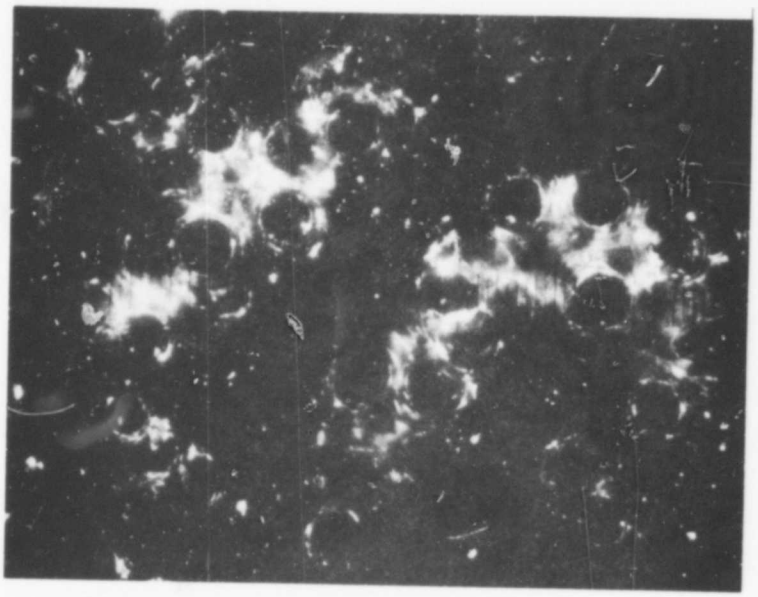

(a) AFTER 15 SECONDS

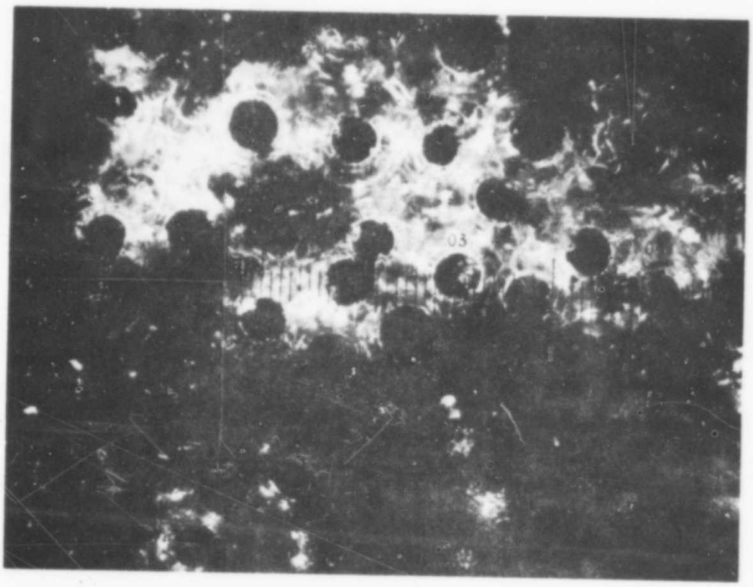

(b) AFTER 60 SECONDS

FIGURE 23 APPEARANCE OF THE SURFACE OF SPECIMEN G2 (110X)

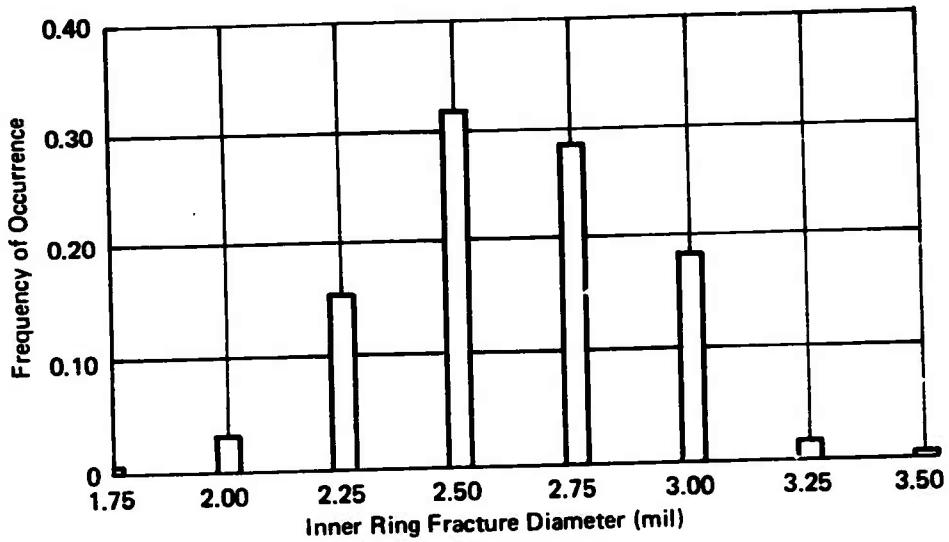

Figure 24. Distribution of Diameters of Ring Fractures in Specimen G2

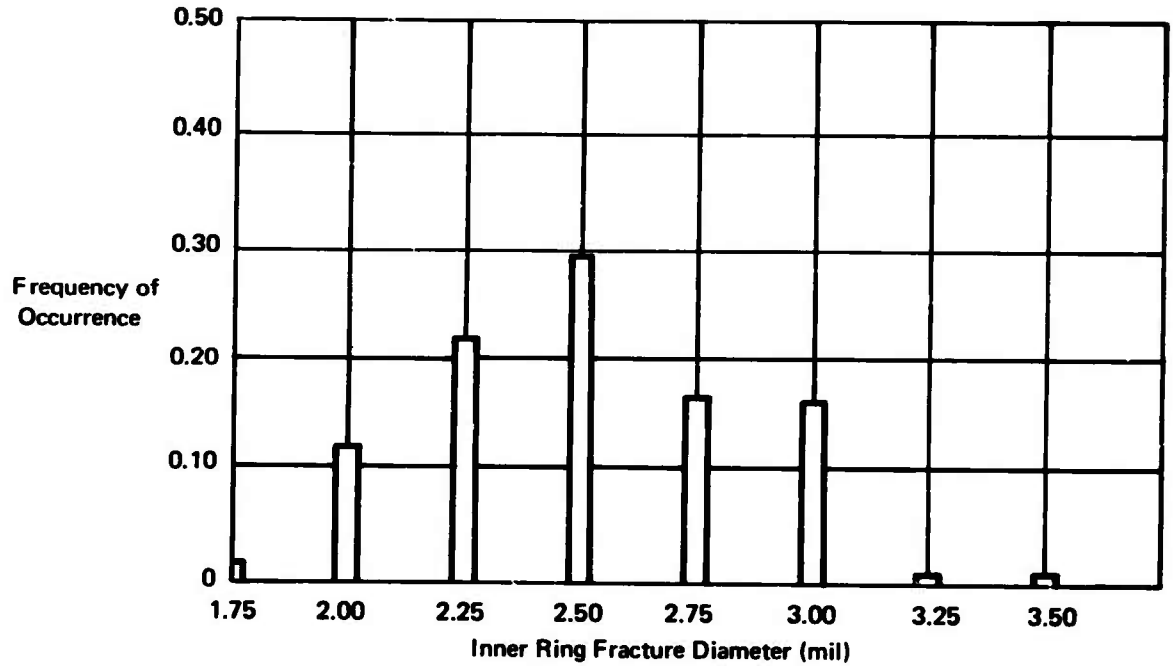

Figure 25. Distribution of Diameters of Ring Fracture in Specimen G3

reaching a maximum value within the given time range. The probability for the formation of ring fractures is quite high under these impact conditions. From these data it is seen that the maximum number of ring fractures is established quite early in the erosion process and that a majority of the rings formed survive the subsequent bombardment of particles as the erosion process continues. The reasons for the difference in the density of cone fractures between the two specimens and the removal of certain cones have been established from the experimental observations. The explanation is illustrated in Figure 26. The top surface appears as in Figure 26a. However, a cross section of the conical fracture surfaces indicates that cones A and C intersect below cone B. Such conditions have been observed microscopically. Cone B is only partially attached to the bulk material while cones A and C are firmly anchored. The colliding particles are capable of producing fractures around cone B while weakening its existing support and it ultimately breaks loose. The depth D is found to be fairly constant over the entire eroded area. In specimen G2 D is approximately 50-60 microns while in specimen G3 the depth D is generally 80 to 90 microns. The larger D in specimen G3 is attributed to the higher velocity of approach. It is the greater depth of fracture penetration for specimen G3 which contributes to the marked difference in ring fracture density when compared with specimen G2.

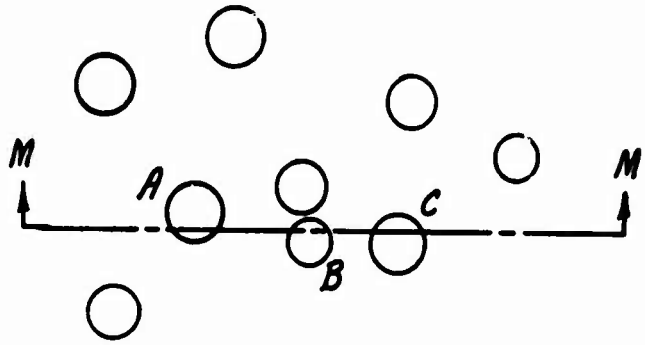

(a) RING FRACTURES ON GLASS SURFACE

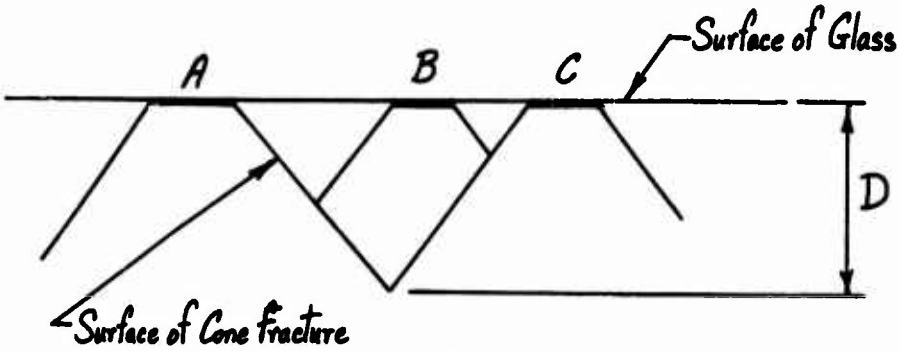

(b) ENLARGEMENT OF SECTION MM

FIGURE 26 MECHANISM FOR REMOVAL OF CONE FRACTURES FROM SURFACE

Following the erosion process in specimen G2 it is seen that around an exposure time of 90 seconds large-scale removal of material from the interstitial regions between the firmly-anchored truncated cones is the primary erosion mechanism. The glass in the interstitial areas is severely fractured and sizable areas are removed during each time increment. The micrograph in Figure 27 illustrates this process. Just above the center of Figure 27 there is a triplet of cones from which the interstitial glass has been removed. In the vicinity of the triplet the imprint of two cones which did not survive the impact loadings are also clearly visible. The conditions for their disintegration correspond to that shown schematically in Figure 26. A number of other cones which are going to be removed with the interstitial glass can also be seen in Figure 27. The sequence of micrographs in Figure 28 shows the growth of an eroded area. The cones protruding from the bulk material are not always visible in the micrographs; only the interstitial material is being removed, the cones at this stage are relatively unaffected by the particle impacts. The glass comprising the truncated cones is quite strong and fairly resistant to erosion. A number of areas on the sample surface were observed microscopically during this stage of the erosion process, and it was found that the growth behavior of nucleated regions was quite irregular. At 130 seconds most of the interstitial material was removed from the primary erosion area on the specimen surface as shown in Figure 29. The removal of the interstitial material completes

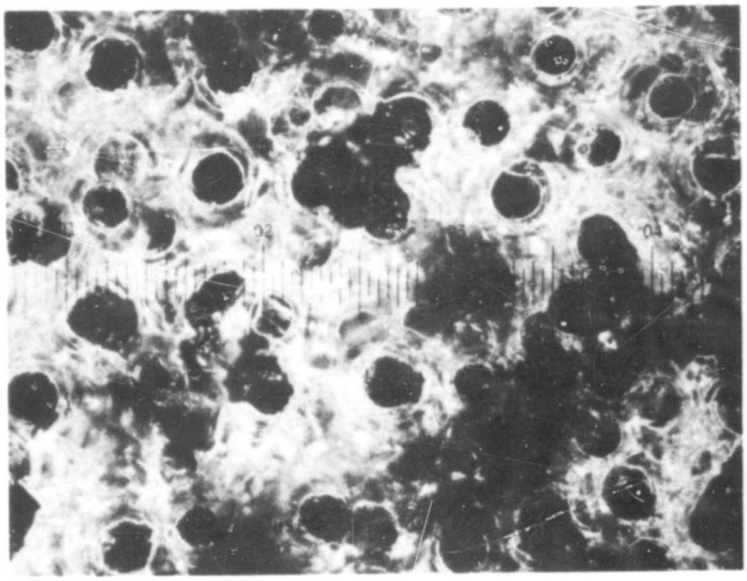

FIGURE 27 REMOVAL OF FRACTURED GLASS FROM INTERSTITIAL REGIONS ON SURFACE OF SPECIMEN G2 (110X)

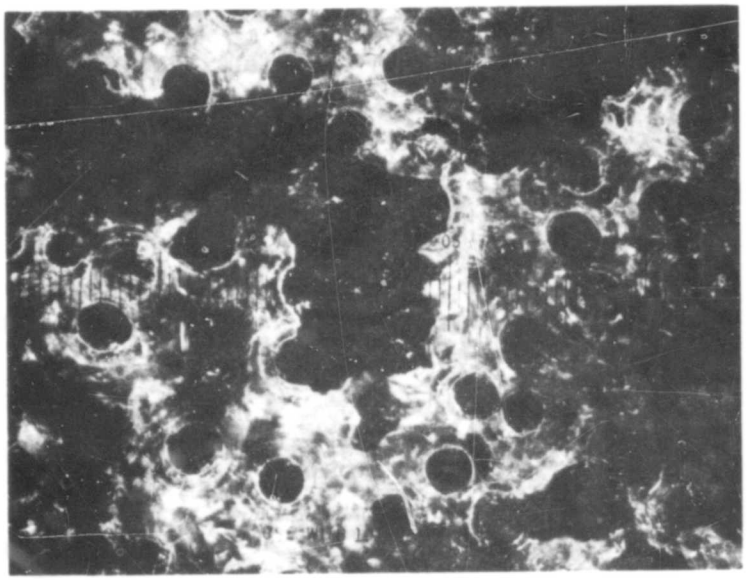

(a) 90 SECONDS

FIGURE 28 GROWTH OF AREA OF INTERSTITIAL GLASS REMOVAL ON SURFACE OF SPECIMEN G2 (110X)

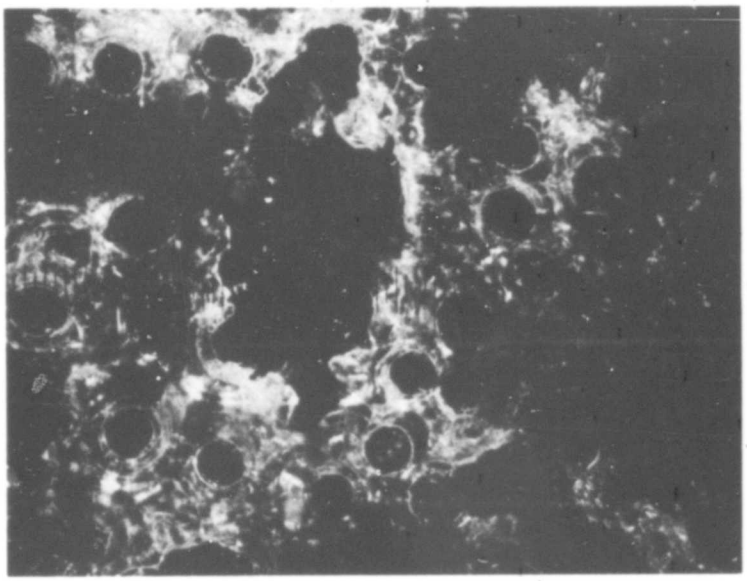

(b) 100 SECONDS

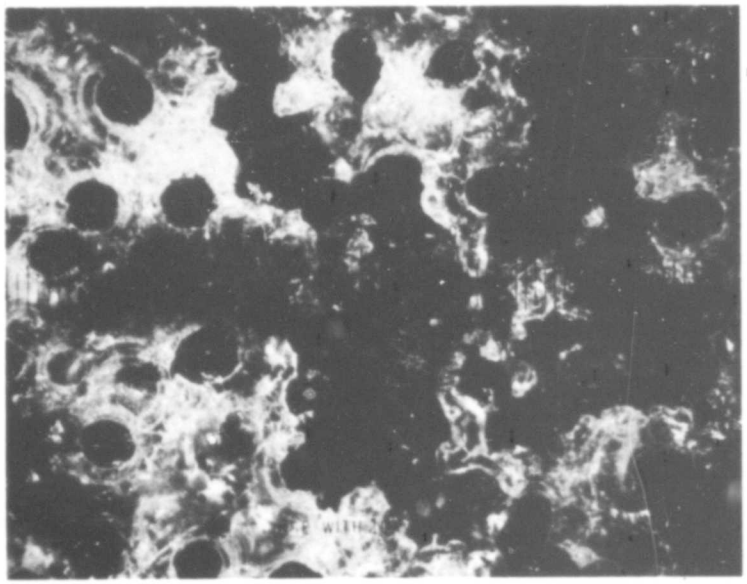

(c) 110 SECONDS

FIGURE 28 GROWTH OF AREA OF INTERSTITIAL GLASS REMOVAL ON SURFACE OF SPECIMEN G2 (110X)

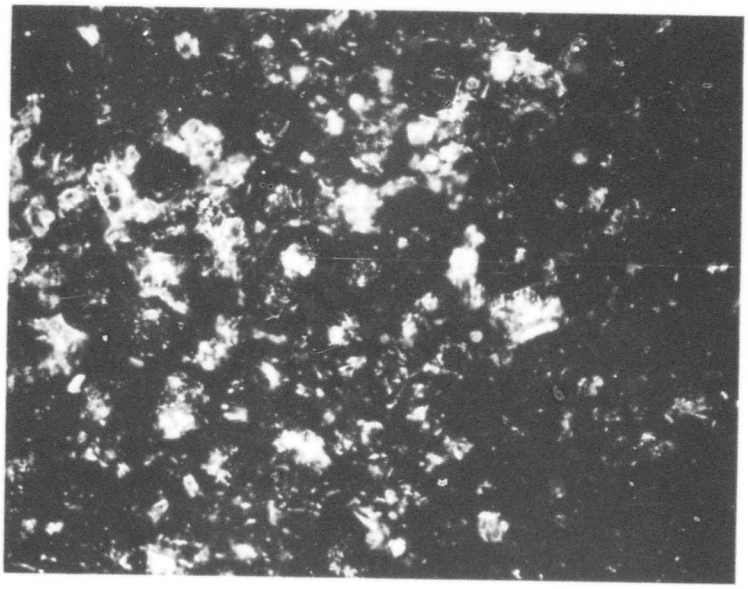

FIGURE 29 APPEARANCE OF ERODED SURFACE OF SPECIMEN G2 AT 130 SECONDS (70X)

another phase of the erosion process which overlaps with the final stage.

The general appearance of the eroded surface is now comparable to a waffle iron. The appearance of the surface of each specimen is shown at lower magnification in Figure 30. Solid cones are protruding from the surface. The impacting particles do little damage in a single impact. The sides of the cones and common points on interaction are highly resistant to material removal. The particles must pulverize the glass in the cones beginning at the plateau and slowly work down to the bulk material (Figure 31). As seen in the plots of the weight-loss data (Figures 11 and 12) this process continues at a uniform rate. No new erosion mechanisms come into play.

The conditions of the glass beads were checked microscopically after colliding with the specimens in the erosion tests, and it was found that no fragmentation of the beads was taking place and that very few fractures could be found on the surface of the beads.

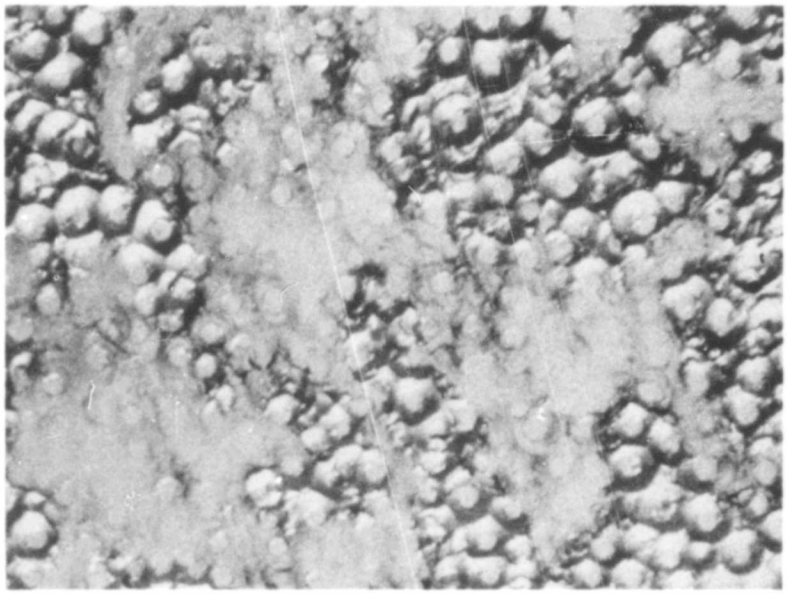

(a) SPECIMEN G2 AT 100 SECONDS (25X)

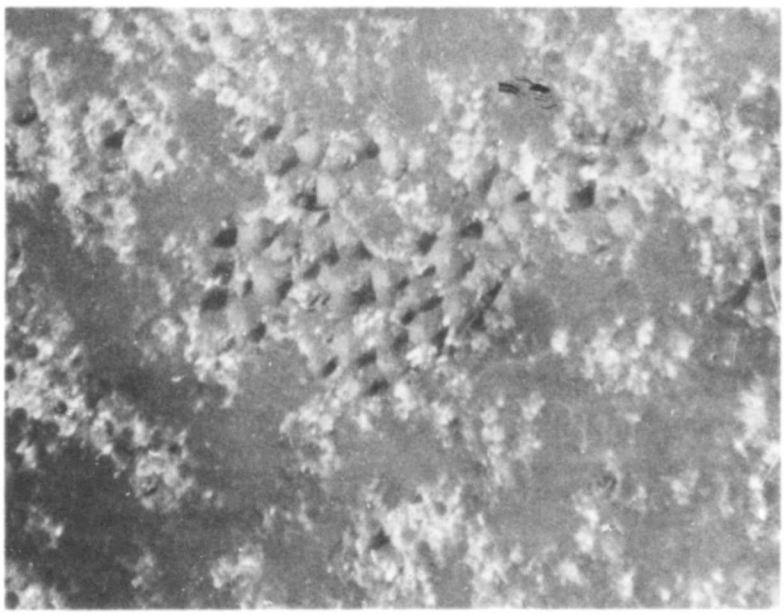

(b) SPECIMEN G3 AT 6 SECONDS (20X)

FIGURE 30 GENERAL APPEARANCE OF ERODED SURFACE OF SPECIMEN G2 AND G3

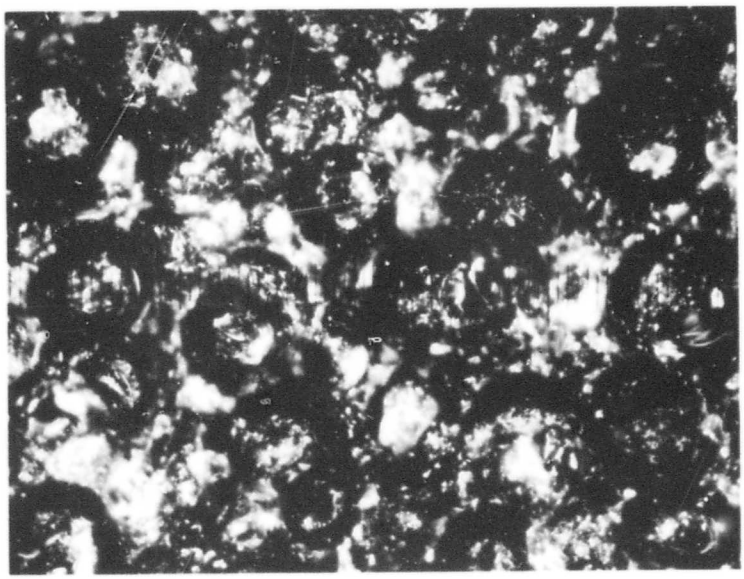

FIGURE 31 APPEARANCE OF ERODED SURFACE OF SPECIMEN G2 AT 305 SECONDS (110X)

VI. GENERAL DISCUSSION

In order to couple the general erosion model developed in Section III with the erosion behavior of specific materials, an experimental procedure was devised for evaluating the statistical parameters appearing in the theory for the special case of spherical glass beads colliding with the plane surface of a specimen of fused silica. The experimental results are now available for the future development of the erosion model.

It was pointed out in Section V-A that the applicability of the Hertzian analysis may be questioned on the basis of the assumptions that the contact area be small in comparison to the diameter of the impinging sphere and that the duration of impact be long in comparison to the time it takes stress waves to traverse the impacting bodies. However the Hertzian prediction of the size of the contact area is found to be in reasonable agreement with the experimental observations pertaining to the production of ring fractures on the glass surfaces. In specimen G1 a high probability exists for the formation of single ring fractures approximately 0.9 mils in diameter. According to the Hertz theory the maximum diameter of the contact area will be 0.70 mils. In static loading of indenters on glass plates it is found that ring fractures generally occur outside of the contact area by diameters up to 50 percent[18] greater than the contact diameter.

The usual difference is 10 to 20 percent. The experimental work of Tsai and Kolsky[11] on impact of steel ball bearings with radii ranging from 1/32 to 1/4 inch on plate glass indicates that the fracture stress in the dynamic tests is approximately one-third higher than the static fracture stress. These observations tend to make the calculated radius of the contact area more closely approximate the experimentally-evaluated radius for the ring fractures.

The Hertz theory predicts the diameter of the contact area for specimens G2 and G3 should be about 5 mils. A very high probability was found for the occurrence of multiple ring fractures. The average diameter of the innermost ring was approximately 2.5 mils: the diameter of the outer rings in each case was determined from the experiments to be slightly larger than the calculated value for the diameter of the contact area. The comparison between theory and experiment is reasonable. The stress generated at an intermediate stage of the compression phase of the impact is sufficient to initiate ring fractures, but the magnitude of the load continues to act along with the expansion of the contact area. Additional ring fractures are produced as a larger area reaches the critical stress level. The process stops when the maximum contact area is reached where it is still possible for a crack to develop just outside this region before the magnitude of the load begins to subside. The static experiment of Sheldon and Finnie[8] for the variation of the center of

approach of a 1/8 inch steel ball on a glass plate indicates that Hertzian expression for the approach distance, Eq. (14) deviates from the experimental value by only 25 percent when the applied load is more than 120 times the load for the initial ring fracture. It thus appears that cracked material will transmit load. Sheldon and Finnie state that this is due to the fact that the stresses in the contact region are primarily compressive.

Only indirect evidence can be provided in regard to the second assumption of the Hertz theory. According to the calculation of the dynamic contact stresses at the boundary of the area of contact provided by Tsai[19], it is seen that the radial tensile stress component is essentially equal to the Hertzian radial tensile stress for a maximum radius of contact less that 10 mils independent of the duration of contact. The size of the contact areas found experimentally are considerably smaller than this value.

The measurements of the ring fractures would tend to support the Hertzian evaluation of the contact stresses for the impact conditions appropriate to the erosion tests conducted in this report. The Hertzian expression for the contact stresses will therefore be used to construct an appropriate fracture criterion for the small bead sizes used in the experimental program. This task will be considered in future work.

Two additional observations can be made pertaining to ring fractures based on these initial studies. First, the semi-angle of the conical fracture surfaces exposed in the intermediate stage of the erosion of specimens G2 and G3 appeared to be closer to 45° rather than 65.5° in fused silica as measured by Benbow[20]. Secondly, the anomolous occurrence of 3 mil ring fractures on the surface of specimen G1 cannot be explained. Their existence is not at all in conformity with the Hertzian theory. The 3 mil ring fractures were incorrectly taken to be the principal element contributing to the nucleation of large-scale pit growth on the surface. The number and configuration of the 3 mil ring fractures was tabluated after each erosion increment, until it was discovered that an exposure time was reached when no new 3 mil ring fractures were being formed. It then became evident that the smaller ring fractures described above were the primary mechanism of material removal.

Very small pieces of material were removed along the periphery of the 0.9 mil rings. Once a region began to develop, these rings overlapped each other and exhibited the form of preferential growth described by the theory. They were found to cluster in the neighborhood of the 3 mil rings. The complex spatial growth pattern was difficult to tabulate by the procedures established for the anticipated erosion damage on a somewhat larger scale. The depth of the surface layer removed was only five to ten microns, so the erosion of layers below the

surface layer was nearly impossible to follow. The chipping associated with the ring fracture was responsible for material removal for almost the full duration of the cummulative erosion time. Ring fractures were still being formed on the eroded surface just prior to the attainment of the steady-state erosion rate (Figure 10). When the steady-state erosion rate was attained, material removal took place by fine-scale chipping of pieces from the highly-flawed surface without any evidence of the ring formations.

Finnie[21] developed a model for the erosion of brittle materials based on the idea that the volume removed per spherical bead impact V_p, is proportional to the product of the statistical average of the square of the outermost ring crack $(\overline{a^{*2}})$, and the depth of the inner ring fracture. Using the statistical flaw theory of Oh and Finnie[12] and the usual Hertzian relations, Finnie finds

$$V_p \propto Rv^{4/5} (\overline{a^{*2}}) = F \qquad (24)$$

The experimental confirmation of this result based on the erosion of glass indicates that the linear proportionality of V_p with F, the grouping of parameters in Eq. (24), was not upheld, although the data did cluster along a straight line with a slope of 1.30 on a log-log plot of V_p vs F.

If V_p is evaluated by the conventional solid particle erosion tests, it would presumably correspond to the steady-state rate of erosion. Eq. (24) in essence relates conditions in the very early stages of the erosion process to measurements of the volume removed (or equivalently, weight loss) in the later stages of the erosion process. According to the erosion mechanism studies for fused silica, it is seen that Finnie's model is representative of the primary mechanism for material removal in specimen G1 over the entire period of exposure. However, the erosion of specimen G2 and G3 involves several erosion mechanisms. The prevalent mechanism, chipping of the conical frustum population, for the steady-state region of the weight loss data (Figures 11 and 12) is entirely different from the ring fracture mechanism which is the basis of Finnie's model. In this case agreement between the experimental and calculated values of V_p would be fortuitous.

These initial experiments in this report have provided valuable insights into the role of particle size and velocity on the erosion characteristics of inorganic glasses. These experimental observations will be used in conjunction with the available Hertzian analyses of impact phenomena to further advance the quantitative theory of erosion of brittle materials.

VII. CONCLUSIONS

The initial studies on analytical modeling of solid particle erosion have demonstrated that it is feasible to include more details of the erosion behavior of materials in the general statistical framework which is developed in this report. This is possible through simplification of the impact conditions, direct microscopic observation of the time evolution of erosion damage on material surfaces, and the preliminary observation that the Hertzian theory may be applicable to impact conditions on a scale appropriate to solid particle erosion.

At the present time there is a general lack of experimental results pertaining to the critical velocity for fracture of inorganic glasses and other brittle materials when impacted by spherical particles less than 24 mils in diameter. This size of impacting particle is approaching the upper limit of particle sizes which are of interest in investigation of sand erosion. Tests are being planned for evaluating the most probable value of the critical velocity for fracture as a function of particle sizes in the range from 1 to 18 mils using the AFML-Bell erosion apparatus for the materials which are selected for study in this research. The quantitative evaluation of the critical velocity is required for obtaining analytical representations of the primary erosion mechanisms which can be incorporated into the functional forms of the pit nucleation and growth functions.

In conjunction with the detailed studies of direct impacts, a series of controlled experiments are planned to progressively increase the complexity of the loading conditions using the AFML-Bell erosion apparatus. This effort is intended to extend the range of application of the theoretical predictions to conditions which are of greater interest in solid particle erosion. The impact conditions to be considered are oblique impacts, impacts by arbitrarily-shaped particles, higher velocity impacts, and finally erosion by liquid drops. More complex forms of material behavior than that of the inorganic glasses will also be investigated once viable predictive tools are available.

APPENDIX

COMPUTER PROGRAM FOR ANALYTIC MODELING

The system of equations governing the erosion of solid surfaces by the nucleation and growth of erosion pits, Eq. (11), are programmed for digital computer computations. The specific input data for the program provided is highly restricted in order to make it explicit. There is no difficulty in including a very broad range of input functions now that means are available for evaluating the integrals in Eq. (11). The form of the output from the computer computations is also arbitrary.

Generalized forms of the program would include a different nucleation probability function and growth rate function for each of the eroding layers whose thickness can be varied as material is removed from the bulk solid. Since it is our purpose to specify this information based on experimental and theoretical considerations appropriate to realistic material behavior and impact conditions, relatively simple forms of the input data were selected to check if the program was operational. This has been verified assuming the relevant functions are identical for all layers of the laminate model which are all the same thickness. Identical linear growth rates are assumed in both lateral directions on the surface of the eroding solid, and the pit nucleation function is simply proportional to the exposure time.

```
      DIMENSION G(50),GG(50),A(2,1001),Y1(1001),Z1(1001),AE(1001)
      DIMENSION TERM(2),GRAD(1001),GR(2,1001)
      READ(5,9) TE,TD
    9 FORMAT(2E16.8)
      READ(5,10) TH,TL,ETA,AC
   10 FORMAT(4E16.8)
      NMAX=TH/TL
      MMAX=TE/TD&1.
      READ(5,11) (G(I),GG(I),I=1,NMAX)
   11 FORMAT(2E16.9)
      WRITE(6,12) AC,TH,TL,ETA,TE,TC
   12 FORMAT(10X,14HORIGINAL AREA=,F12.8,/,10X,10HTHICKNESS=,F12.8,/,
     110X,17HLAMINA THICKNESS=,F12.8,/,10X,13HSHAPE FACTOR=,F12.8,/,
     210X,13HEROSION TIME=,F12.8/,10X,15HTIME INCREMENT=,F12.8,//)
      N=0
  100 N=N&1
      IF(N.GT.NMAX) GO TO 300
      WRITE(6,13) N
   13 FORMAT(10X,12HLAYER NUMBER,I3)
      WRITE(6,15) G(N),GG(N)
   15 FORMAT(10X,12HGROWTH RATE=,F12.8,/,10X,18HNUCLEATION FACTOR=,F12.8
     1,/)
      WRITE(6,14)
   14 FORMAT(5X,8HSTEP NO.,4X,4HTIME,7X,11HERODED AREA,7X,12HEROSION RAT
     1E/)
      GS=G(N)*G(N)
      IF(N.GT.1) GO TO 50
      A(1,1)=A0
      A(2,1)=0.
      Y1(1)=0.
      Z1(1)=0.
      DO 20 MM=2,MMAX
      A(1,MM)=A0
      A(2,MM)=0.
      RMM=MM-1
      T=RMM*TD
      DO 21 JP=1,2
      DO 22 JL=2,MM
      RJL=JL-1
      TAL=RJL*TD
      Y1(JL)=(T-TAL)*(T-TAL)*TAL*A(JP,JL)
   22 CONTINUE
      IF(MM.GT.2) GO TO 23
      Z1(2)=0.5*TD*Y1(2)
      GO TO 24
   23 CALL QSF(TD,Y1,Z1,MM)
   24 TERM(JP)=Z1(MM)
   21 CONTINUE
      AE(MM)=ETA*GS*GG(N)*(TERM(1)-TERM(2))
      A(2,MM)=AE(MM)
   20 CONTINUE
      GRAD(1)=0.
      GR(2,1)=0.
      AE(1)=0.
      GRAD(2)=AE(2)/TD
      GR(2,2)=GRAD(2)
      WRITE(6,25) TC,AE(2),GR(2,2)
```

```
25 FORMAT(10X,1H2,4X,F8.4,2X,E16.8,2X,E16.8)
   CALL DET3(TD,AE,GRAD,MMAX,MCDE)
   DO 26 KP=3,MMAX
   RKP=KP-1
   T=RKP*TD
   GR(2,KP)=GRAD(KP)
   WRITE(6,27) KP,T,AE(KP),GR(2,KP)
26 CONTINUE
27 FORMAT(6X,I5,4X,F8.4,2X,E16.8,2X,E16.8)
   GO TO 100
50 AE(1)=0.
   GR(1,1)=0.
   DO 30 MM=2,MMAX
   GR(1,MM)=GR(2,MM)
   GR(2,MM)=0.
   RMM=MM-1
   T=RMM*TD
   DO 31 JP=1,2
   DO 32 JL=2,MM
   RJL=JL-1
   TAL=RJL*TD
   Y1(JL)=(T-TAL)*GR(JP,JL)
32 CONTINUE
   IF(MM.GT.2) GO TO 33
   Z1(2)=0.5*TD*Y1(2)
   GO TO 34
33 CALL QSF(TD,Y1,Z1,MM)
34 DO 35 IL=2,MM
   RIL=IL-1
   TOU=RIL*TD
   Y1(IL)=(T-TOU)*Z1(IL)
35 CONTINUE
   IF(MM.GT.2) GO TO 36
   Z1(2)=0.5*TD*Y1(2)
   GO TO 37
36 CALL QSF(TD,Y1,Z1,MM)
37 TERM(JP)=2.0*ETA*GS*GG(M)*Z1(MM)
31 CONTINUE
   GR(2,MM)=TERM(1)-TERM(2)
   AE(MM)=AE(MM-1)+GR(2,MM)*TD
   WRITE(6,38) MM,T,AE(MM),GR(2,MM)
30 CONTINUE
38 FORMAT(6X,I5,4X,F8.4,2X,E16.8,2X,E16.8)
   GO TO 100
300 STOP
   END
```

```
      SUBROUTINE QSF(H,Y,Z,NDIM)

      DIMENSION Y(100),Z(100)

      HT=.1333333*H
      IF(NDIM-5)7,8,1

    1 SUM1=Y(2)&Y(2)
      SUM1=SUM1&SUM1
      SUM1=HT*(Y(1)&SUM1&Y(3))
      AUX1=Y(4)&Y(4)
      AUX1=AUX1&AUX1
      AUX1=SUM1&HT*(Y(3)&AUX1&Y(5))
      AUX2=HT*(Y(1)&3.875*(Y(2)&Y(5))&2.625*(Y(3)&Y(4))&Y(6))
      SUM2=Y(5)&Y(5)
      SUM2=SUM2&SUM2
      SUM2=AUX2-HT*(Y(4)&SUM2&Y(6))
      Z(1)=0.
      AUX=Y(3)&Y(3)
      AUX=AUX&AUX
      Z(2)=SUM2-HT*(Y(2)&AUX&Y(4))
      Z(3)=SUM1
      Z(4)=SUM2
      IF(NDIM-6)5,5,2
C
C     INTEGRATION LOOP
    2 DO 4 I=7,NDIM,2
      SUM1=AUX1
      SUM2=AUX2
      AUX1=Y(I-1)&Y(I-1)
      AUX1=AUX1&AUX1
      AUX1=SUM1&HT*(Y(I-2)&AUX1&Y(I))
      Z(I-2)=SUM1
      IF(I-NDIM)3,6,6
    3 AUX2=Y(I)&Y(I)
      AUX2=AUX2&AUX2
      AUX2=SUM2&HT*(Y(I-1)&AUX2&Y(I&1))
    4 Z(I-1)=SUM2
    5 Z(NDIM-1)=AUX1
      Z(NDIM)=AUX2
      RETURN
    6 Z(NDIM-1)=SUM2
      Z(NDIM)=AUX1
      RETURN
C     END OF INTEGRATION LOOP
C
    7 IF(NDIM-3)12,11,8
C
C     NDIM IS EQUAL TO 4 OR 5
    8 SUM2=1.125*HT*(Y(1)&Y(2)&Y(2)&Y(2)&Y(3)&Y(3)&Y(3)&Y(4))
      SUM1=Y(2)&Y(2)
      SUM1=SUM1&SUM1
      SUM1=HT*(Y(1)&SUM1&Y(3))
      Z(1)=0.
      AUX1=Y(3)&Y(3)
      AUX1=AUX1&AUX1
```

```
      Z(2)=SUM2-HT*(Y(2)&AL>1&Y(4))
      IF(NDIM-5)10,9,9
    9 AUX1=Y(4)&Y(4)
      ALX1=AU>1&ALX1
      Z(5)=SUM1&HT*(Y(3)&AL>1&Y(5))
   10 Z(3)=SUM1
      Z(4)=SUM2
      RETURN
C
C     NDIM IS EQUAL TO 3
   11 SUM1=HT*(1.25*Y(1)&Y(2)&Y(2)-.25*Y(3))
      SUM2=Y(2)&Y(2)
      SUM2=SUM2&SUM2
      Z(3)=HT*(Y(1)&SUM2&Y(3))
      Z(1)=0.
      Z(2)=SUM1
   12 RETURN
      END
```

```
      SUBROUTINE DET3(H,Y,Z,NDIM,IER)
      DIMENSION Y(100),Z(100)
      IF(NDIM-3) 4,1,1
    1 IF(H) 2,5,2
    2 HH=0.5/H
      YY=Y(NDIM-2)
      B=Y(2)&Y(2)
      B=HH*(B&B-Y(3)-Y(1)-Y(1)-Y(1))
      DO 3 I=3,NDIM
      A=B
      B=HH*(Y(I)-Y(I-2))
    3 Z(I-2)=A
      IER=0
      A=Y(NDIM-1)&Y(NDIM-1)
      Z(NDIM)=HH*(Y(NDIM)&Y(NDIM)&Y(NDIM)-A-A&YY)
      Z(NDIM-1)=B
      RETURN
    4 IER=-1
      RETURN
    5 IER=1
      RETURN
      END
```

REFERENCES

1. F. J. Heymann, On The Time Dependence of the Rate of Erosion Due to Liquid Impact or Cavitation, Report E-1448, Steam Divisions Engineering, Westinghouse Electric Corp., June, 1966.

2. _____, "On the Time Dependence of the Rate of Erosion Due to Impingement or Cavitation", Erosion by Cavitation or Impingement, ASTM STP 408 (1967) p.70.

3. H. Hertz, "On the Contact of Elastic Solids", Miscellaneous Papers, London: MacMillan and Company, 1896; p.142.

4. _____, "On the Contact of Rigid Elastic Solids and on Hardness", Miscellaneous Papers, London: MacMillan and Company, 1896; p. 163.

5. M. T. Huber, Annln. Phys. 14 (1904) 153.

6. S. Timoshenko and J. N. Goodier, Theory of Elasticity (second edition), New York: McGraw-Hill Book Company, Inc., 1951.

7. W. Goldsmith, Impact, London: Edward Arnold Ltd., 1960.

8. G. L. Sheldon and I. Finnie, "The Mechanism of Material Removal in the Erosive Cutting of Brittle Materials", Trans. ASME, 88B (1966) 393.

9. F. Auerbach, Ann. Phys. Chem., 43 (1891) 61.

10. F. C. Roesler, "Indentation Hardness of Glass as an Energy Scaling Law", Proc. Phys. Soc. (London) B69 (1956) 55.

11. Y. M. Tsai and H. Kolsky, "A Theoretical and Experimental Investigation of the Flaw Distribution on Glass Surfaces," J. Mech. Phys. Solids, 15 (1967) 29.

12. H. L. Oh and I. Finnie, "The Ring Cracking of Glass by Spherical Indenters", J. Mech. Phys. Solids, 15 (1967) 401.

13. G. M. C. Fisher, "The Auerbach Range in the Hertizan Fracture of Glass", J. Appl. Phys., 38 (1967) 1781.

14. F. C. Frank and B. R. Lawn, "On the Theory of Hertzian Fracture", Proc. Roy. Soc. (London), A 299 (1967) 291.

15. F. B. Langitan and B. R. Lawn, "Hertzian Fracture Experiment on Abraded Glass Surfaces as Definitive Evidence for an Energy Balance Explanation of Auerbach's Law," J. Appl. Phys., 40 (1969) 4009.

16. C. J. Phillips, "The Strength and Weakness of Brittle Materials", American Scientist, 53 (1965) 20.

17. J. P. Andrews, "Observations on Percussion Figures", Proc. Phys. Soc. (London) 43 (1931) 18.

18. J. P. A. Tillett, "Fracture of Glass by Spherical Indenters" Proc. Phys. Soc. (London) B69 (1956) 47.

19. Y. M. Tsai, "Dynamic Contact Stresses Produced by the Impact of An Axisymmetrical Projectile on an Elastic Half-Space," Int. J. Solids Structures, 7 (1971) 543.

20. J. J. Benbow, "Cone Cracks in Fused Silica," Proc. Phys. Soc. (London), 75 (1960) 697.

21. I. Finnie, Study of the Mechanisms of Sand and Dust Erosion, USAA VLABS Technical Report 70-70 (December, 1970).